POLITECNICO
MILANO 1863

SCUOLA DI INGEGNERIA INDUSTRIALE
E DELL'INFORMAZIONE

Quasi-Periodic Orbital Families Performance Analysis for Exoplanets Observation by means of Telescope-Occulter Formation Flying

Master of Science in
Space Engineering

Author: **Giorgia Biagetti**

Student ID: 970943
Advisor: Prof. Michèle Lavagna
Co-advisors: Daniele Barberi Spirito
Academic Year: 2021-22

Abstract

The study of extra-solar planets represents one of the most ambitious goals to be reached in space science in the near future. Thanks to indirect detection techniques, such as radial velocity-based, transits and gravitational microlensing, the list of known exoplanets has rapidly grown over the years. However, only direct investigation allows a detailed view of their actual characteristics, like atmospheric composition, physical and orbital properties, and eventually evidence of life. Nevertheless, the enormous contrast between the parent star and the planet imposes strong constraints on this kind of observations, especially in terms of required angular separation. This study presents a shader concept for exoplanets imaging, based on the Formation Flying of two small spacecrafts placed on QPOFs: an occulter designed to provide adequate starlight suppression within its shadow and a conventional telescope to collect the light from the target planet. The primary objective of this work is to propose optimal Periodic orbital and attitude configurations to perform an exoplanet observation mission using the coronagraph method in a Sun-Earth, non-Keplerian framework.

Keywords: External Occulter Design, Quasi-Periodic Orbital Families (QPOFs), Coronagraph Method, Exoplanets Direct Imaging

Abstract in lingua italiana

Lo studio degli esopianeti rappresenta uno degli obiettivi più ambiziosi da raggiungere nel campo dell' ingegneria spaziale nel prossimo futuro. Grazie alle tecniche di rilevamento indiretto, come la velocità radiale, i transiti e il metodo di microlente gravitazionale, l'elenco degli esopianeti conosciuti è rapidamente aumentato nel corso degli anni. Tuttavia, solo l'indagine diretta consente una visione dettagliata delle loro reali caratteristiche, come la composizione dell'atmosfera, le proprietà fisiche ed orbitali ed, eventualmente, la presenza di vita. Inoltre, l'enorme contrasto tra la stella madre e il pianeta impone forti vincoli su questo tipo di osservazioni, soprattutto in termini di separazione angolare richiesta. Questo studio presenta un metodo di occultamento per l'imaging degli esopianeti, basato sull'utilizzo di due satelliti in formazione posizionati su Famiglie Orbitali Quasi-Periodiche: un occultatore progettato per fornire una adeguata soppressione della luce stellare all'interno della sua ombra e un telescopio per raccogliere la luce del pianeta target. L'obiettivo principale di questo lavoro è quello di proporre configurazioni orbitali periodiche ottimali per eseguire una missione di osservazione degli esopianeti utilizzando il metodo del coronografo in un contesto non-Kepleriano Sole-Terra.

Parole chiave: Design Occultatore Esterno, Famiglie Orbitali Quasi-Periodiche, Metodo Coronografo, Rilevamento diretto di Esopianeti

Contents

List of Figures

List of Tables

Nomenclature

ADCS	Attitude Determination and Control System
AU	Astronomical Unit
CoM	Center of Mass
CR3BP	Circular Restricted 3-Body Problem
CR	Contrast Ratio
EoM	Equations of motion
FoV	Field of View
GC	Galactic Center
HZ	Habitable Zone
IWA	Inner Working Angle
L2	Lagrangian Point L2
LoS	Line of Sight
NBP	N-Body Problem
OSC	Occulter Spacecraft
QPOFs	Quasi-Periodic Orbital Families
RV	Radial Velocity
SNR	Signal to Noise Ratio
SP	Solar Panel
TSC	Telescope Spacecraft

1 | Introduction

The study of exoplanets is an important and exciting area of space science research. Direct observation of exoplanets is crucial to understand their physical and orbital properties, as well as the potential for life. However, observing exoplanets is challenging due to the enormous luminosity contrast between the parent star and the planet itself, which makes it difficult to obtain clear images.

In the past few decades, space Telescopes have revolutionized our understanding of exoplanets. Previous missions have discovered and characterized numerous transiting systems, greatly expanding our knowledge of exoplanets abundance and diversity. *Spitzer Space Telescope* [1], retired in January 2020 after operating for over 16 years and *Kepler* [2], launched in 2009, ended its primary mission in 2013 due to two reaction wheels failure, then extended and renamed as *K2*, which operated from 2014 to 2018 before it was decommissioned. The *Hubble Space Telescope* [3], launched in 1990, is still operating and continues to make groundbreaking observations of the universe.

More recently, the *Transiting Exoplanet Survey Satellite* (TESS) [4] was launched successfully in 2018. TESS is expected to discover thousands of new exoplanets, particularly in nearby systems, and will provide targets for future follow-up observations. The *James Webb Space Telescope* (JWST) [5], launched in 2022, is set to revolutionize our understanding of exoplanet atmospheres through mid-infrared transit spectroscopy and direct imaging of young massive exoplanets.

Another upcoming mission is the *Nancy Grace Roman Space Telescope* [6], set to be launched in the mid-2020s. The Roman will include a high-contrast internal coronagraph instrument (CGI) that will be capable of directly imaging a significant number of known exoplanets, allowing the characterization of exoplanets with an unprecedented level of detail.

Pending the recommendations of the 2021 Decadal Survey [7], a Star-shade could be launched to rendezvous with Roman, enabling the direct imaging of Earth-like exoplanets. If recommended, large-scale missions such as *LUVOIR* (Large UV/Optical/IR) Surveyor [8] and *HabEx* (Habitable Exoplanet Imaging Mission) [9] will have the capacity to directly image and spectrally analyze Earth-like exoplanets, survey nearby stars to gauge the prevalence of such planets, and search for the spectral signature of gases such as water

vapor and oxygen, which could indicate the existence of life.

Additionally, the *Origins Space Telescope* (OST) [10] plans to measure the atmosphere of rocky exoplanets transiting M dwarfs and directly image cool gas giants. If approved, any of these missions would have the capability to uncover compelling evidence indicating the presence of life on remote planets.

Despite the success of these missions, they all share one major drawback: they are expensive and complex. This is particularly true for missions that use large spacecrafts. In fact, no exoplanets observation mission has ever flown using small CubeSats. Therefore, this thesis proposes a new method for exoplanet observation that studies a formation of two small spacecrafts, a Telescope and an Occulter, placed respectively on periodic and quasi-periodic orbits to exploit natural dynamics and reduce costs even further.

It is worth mentioning that the external Occulter or Star-shade method has several advantages over other techniques for exoplanets observation. One advantage is that it can suppress the starlight to very high contrast ratios, allowing the detection of faint exoplanets that would be difficult to observe otherwise. Another benefit is that it can operate at a wide range of wavelengths, allowing for the observation of a variety of exoplanet types. Additionally, this method is less sensitive to instrument and Telescope imperfections, making it a more robust technique. The use of two spacecrafts, with one acting as the Occulter and the other as the Telescope, also provides flexibility in terms of the mission design and allows for easier maintenance and upgrades.

Overall, the coronagraph method with two spacecrafts could provide high-quality, high-contrast images of exoplanets and enable the study of their atmospheres and physical properties.

1.1. State of Art

The discovery of extra-solar planets has been one of the most exciting astronomical findings in the last decades. It has proved that studying planetary evolution, insights on Solar System formation can be retrieved.

Observations of habitable exoplanets are of particular interest. Those planets located outside of our solar system have the potential to support life as we know it. These exoplanets orbit stars other than our sun, and some of them are located within the so called *Habitable Zone* (HZ), which is the range of distances where the temperature is optimal for liquid water to exist on the planet surface.

The presence of liquid water is considered a key factor in determining the habitability of an exoplanet, as it is essential for the development of life. However, many other factors come into play, including its atmospheric composition, the presence of a magnetic field, and the stability of its orbit.

Nowadays several direct and indirect methods [11] have been used to study these interesting celestial objects. In Figure 1.1 the total number of exoplanets discovered with different methods over the years is illustrated.

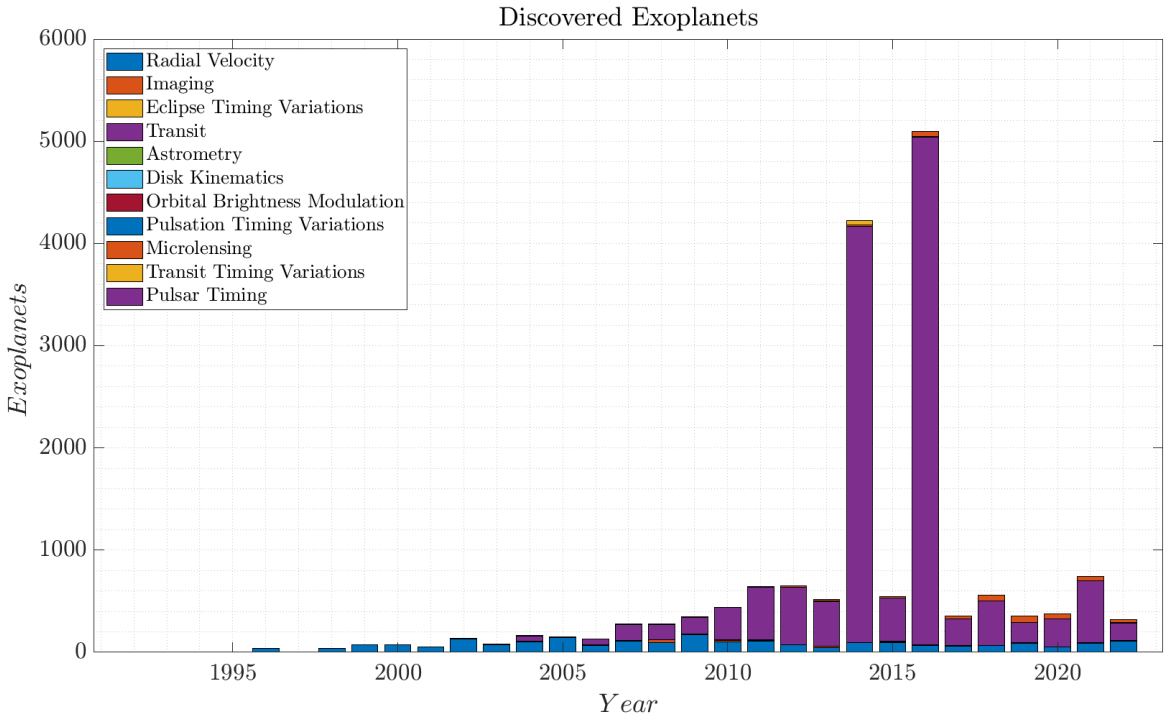

Figure 1.1: Exoplanets discovered over the past twenty years using different techniques.

1.1.1. Indirect methods

Indirect observation methods are essential tools used in astronomy to study objects that are too far away or too small to be observed directly. This includes many of the most fascinating and mysterious objects in the universe, such as black holes, neutron stars, and exoplanets. Indirect methods involve measuring the effects that these objects have on their surroundings, such as the gravitational pull they exert on nearby objects, the way they distort light rays, or the changes they induce in the motion of their host stars. By carefully analyzing these subtle effects, astronomers can get useful insights about the properties, behavior, and evolution of these distant objects. Indirect methods have revolutionized our understanding of the universe, and continue to be a crucial tool in the search for answers to some of the most profound questions in science. Here are several commonly employed techniques for indirectly observing exoplanets.

- **Astrometry**. Astrometric methods are based on perturbations of the star motion. The advantage of these techniques is that they do not depend on the angle between the orbital plane and the LoS (Line of Sight), but they are effective only for large mass planets orbiting at some distance from their parent stars.
- **Doppler method**. About 450 exoplanets have been discovered by studying the periodic changes of the radial velocities (RV) of stars, indicating that they have massive invisible companions. The method reveals only Jupiter-like planets, while smaller ones are too light to cause detectable perturbations. Moreover, if the orbital plane is almost perpendicular to the LoS, Doppler shift cannot be perceived.
- **Gravitational microlensing**. Under certain conditions, light rays from a distant background object are bent by the gravitational potential of a foreground object to create distorted images of the source. Relative motion between source, lens and observer leads to time-varying amplification of the images known as microlensing events. Although the method is sensitive also to low mass planets, the occurrence of such an event is very small.
- **Transit**. Given a suitable alignment geometry, light from the host star is attenuated by the transit of a planet across its disk, with the effect repeating at the orbital period. The probability of observing such a transit for any given star is extremely small. On the other side, observing the transit of an exoplanet is much simpler than determining a Doppler shift. Launched in 2019, *Cheops* [12], the Characterising Exoplanet Satellite, was ESA first mission dedicated to the study of exoplanets exploiting transit technique.

- **Timing**. An orbiting planet is accompanied by the periodic oscillation of the position of the host star around the system barycenter. If the star has periodic time signatures then these can provide an alternative route to the dynamical detection of orbiting planets through the change in measured period due to light travel time. There are three classes of object which offer this possibility: radio pulsars, pulsating stars, and eclipsing binaries.

1.1.2. Direct methods

Although indirect methods are fundamental to reveal the presence of exoplanets, only direct observation can give access to their actual characteristics, like atmosphere, physical and orbital properties, and eventually evidence of life. In fact, since the first extra-solar planet *51 Pegasi b* was discovered by a team of astronomers led by Didier Queloz in 1995 [13], various techniques have been used to infer the presence of large planets, but none have the capability to image Earth-like planets directly. Finding terrestrial planets is very challenging due to the extremely large brightness ratio (also called contrast ratio CR) between the planet and the star; in the visible spectrum, the contrast, is approximately 10^{-10} [14]. Moreover, the maximal angular separation between the planet and its star should be in the order of 0.1 *arcsec* for a star located at 10 *pc* from Earth. Several methods [15–18] have proposed to decrease the intensity of starlight within the Telescope, by adjusting the point-spread function so that there is very little starlight at the location of the planet in the image plane of the Telescope. However, while these techniques have demonstrated the potential to provide the necessary contrast, they need an adaptive-optics system within the Telescope to correct aberrations in the wave front (induced largely by imperfect optics), which tend to spill unwanted light into the search area.

To overcome this issue, Spitzer proposed in 1962 a shader concept for exoplanets imaging, called coronagraph method, based on the use of two separate spacecrafts. He realized that two satellites could fly in formation at a great distance in space and provide a shadow deep and wide enough to enable the detection of planets around other stars.

1.1.3. External Coronograph method

One promising technique for imaging exoplanets is the use of an external Occulter, a device that blocks out the bright light from a star to reveal the faint light from any surrounding planets. While both internal and external coronagraphs have been used for this purpose, recent advances have shown that external Star-shades offer several key advantages over their internal counterparts. In the next section the benefits of exploiting two separate

spacecrafts over a single spacecraft for exoplanet observation are discussed.

- **Improved angular resolution**. An improved angular resolution can be achieved by using one spacecraft as the occulting mask while the other spacecraft observes the exoplanet. This arrangement provides a higher angular resolution than what would not be feasible with a single spacecraft.
- **Increased sensitivity**. The sensitivity of the observation can be increased by reducing the amount of light coming from the host star using the Occulter. As a result, exoplanets that are too faint to be detected with a single spacecraft are observable.
- **Better stability**. Two spacecrafts can provide better stability for the observation, which is crucial for accurate measurements of exoplanet properties. One spacecraft can be utilized to observe the exoplanet while the other spacecraft acts as a reference for the observation.
- **Improved measurement of exoplanet properties**. By simultaneously measuring the properties of the exoplanet and the host star, more information can be obtained about the exoplanet itself.
- **Increased observation time**. Using a Telescope - Occulter Formation allows an increase in the amount of observation time, which is advantageous for studying the properties of exoplanets that have long orbital periods.

1.1.4. Telescope Occulter Formation on QPOFs

This study aims at proposing an innovative use of Quasi-Periodic Orbital Families (QPOFs) for Telescope-Occulter Formation, that could provide a significant advantage in the field of exoplanet observation. QPOFs are a unique class of orbits that are periodic in the short term but quasi-periodic in the long term, providing predictable paths for the coronagraphs. By placing the TSC (Telescope Spacecraft) and OSC (Occulter Spacecraft) respectively on a Halo or Lyapunov periodic and quasi-periodic orbital couple, it could be possible to achieve more accurate and efficient exoplanet observations exploiting the natural non-Keplerian dynamics evolution, without increasing mission costs for propellant usage.

QPOFs are also adopted to optimize the observation times and sky coverage. By carefully choosing the orbital parameters of the coronagraph, QPOFs can be used to maximize the time during which the star-exoplanet system is in visibility. This can help increase the amount of data collected during the observation period, and improve the overall quality

of the exoplanet observation.

1.2. The research problem

This research aims at investigating possible scenarios for an exoplanet observation mission through an external Occulter method starting from different scientific requirements. A first selection of all the possible observable targets meeting such requirements is performed. Then, several non-Keplerian families of periodic orbits are generated and selected in order to optimize some performance parameters like sky coverage, time visibility and baseline between TSC and OSC. Consequently, relative attitude dynamics is introduced to better understand the evolution of objects orientation within a three-body problem and verify the high demanding pointing requirements of such a mission. An estimation of the ideal attitude control needed to maintain the formation is finally calculated.

1.2.1. Thesis motivation and Objectives

The discovery and characterization of exoplanets has become a significant focus of scientific research in recent years, and direct observation techniques are crucial for understanding the characteristics of these planets. One promising technique is direct observation via central star occultation, but the high cost and complexity of traditional Telescope - Occulter systems have limited their use in space missions. This thesis aims to explore the potential of Telescope - Occulter orbital and attitude configurations that are more cost-effective and higher-performing for exoplanet observations using the external coronagraph method. The main objectives of this thesis are here listed.

OBJ 1. Investigate the performances of Telescope - Occulter Formation for exoplanets direct observation in non-Keplerian Sun-Earth environment.

OBJ 2. Propose different quasi-periodic orbital configurations in CR3BP (Circular Restricted 3-Body Problem) framework to optimize exoplanets observation using an external Occulter method, reducing mission costs.

OBJ 3. Find sub-optimal TSC and OSC attitude control solutions to reach required LoS pointing accuracy.

OBJ 4. Provide a general methodology and performance guidelines to be used for future Star-shade missions starting from different scientific requirements.

1.3. Thesis Outline

The work presented is organised as follows.

Chapter 2 deals with the background knowledge and recalls mathematical formulations of non-Keplerian dynamical models under study, both for orbital and attitude dynamics. The formulation used to model the Solar Radiation Pressure (SRP) perturbing effect on Euler Equations is recalled. The chapter will also present how generation of Periodic and Quasi-Periodic Halo and Lyapunov orbits has been performed.

Chapter 3 covers the design aspects for an external Occulter mission. The chapter begins by presenting the mission requirements, which include the Occulter-Telescope baseline, star-observer distance and star-exoplanet distance, as well as the observation time and required precision to fullfill mission objectives. Then, results showing all the possible targets satisfying those criteria are presented in order to understand which exoplanets could be observable with a Star-shade method.

The chapter also discusses the mission geometry, specifically the Telescope-Occulter baseline distance, which determines the size of the shadow cast on the Telescope by the Occulter and Inner Working Angle (IWA) needed by the formation. The chapter then moves on to describe the design of the Occulter spacecraft, from both a geometrical and an engineering point of view. Geometric spacecraft design involves creating the Occulter shape based on a mathematical model, while engineering design involves considering various engineering factors such as evaluating the optimal number of petals required to obtain a good diffraction pattern. Overall, the chapter provides a detailed overview of the key considerations and requirements involved in designing a successful external Occulter mission.

Chapter 4 focuses on analyzing and comparing the performance of different Telescope - Occulter orbital configurations for exoplanet observation. It starts by defining the performance metrics for the Telescope-Occulter system, which include target area, visibility time, sky coverage, and it explains why a phase shift between the reference and toroidal orbit is introduced. Then a general comparison between Halo and Lyapunov performances and the optimal orbit configurations are presented. Starting from the optimal orbital solutions, sub-optimal solutions are found introducing attitude dynamics to the problem. The analysis is at this point carried out taking as reference the Telescope-Occulter Formation from *ECLIPSIS* [19] mission. The optimization will return as output the ideal

control torque with and without SRP contribution to the equations of motions. Angular velocities plots for both Telescope and Occulter are examined to check attitude stability. At the end, an evaluation of relative pointing angle between the spacecrafts is assessed to validate the analysis. A table summarizing all the performances for both the orbital families ends the chapter.

Chapter 5 concludes with final remarks and provides a possible roadmap for future research and development.

2 | Background

In this chapter, the background knowledge needed to approach the present research work is recalled. Starting from the CR3BP formulation in Sun-Earth frame, both Halo and Lyapunov periodic orbits are generated exploiting different methods. Once obtained the reference orbits, families of quasi-periodic orbits are computed. Attitude equations of dynamics are then introduced as well as Solar Radiation Pressure disturbance contribution. This chapter aims to build a set of candidates trajectories that will be subsequently evaluated in terms of the performance for the presented study.

2.1. Orbital Dynamics

Dynamical models are often categorized according to the number and nature of the gravitational sources, regardless of the presence of irregular gravity fields or external perturbations. The most general expression of multi-body dynamics is the N-Body Problem. The following equation describes the motion of an object subjected to the gravitational pull of other N-1 objects.

$$\ddot{\mathbf{r}}_i = \sum_{j=1,\ j\neq i}^{N} \nabla \mathbf{U_j} \tag{2.1}$$

where $\nabla \mathbf{U_j}$ is the gravitational attraction exerted from the *j-th* mass. Due to its chaotic and complex behavior, a systematic search of regular motions (such as periodic, quasi-periodic orbits) for the N-Body Problem (NBP) is not possible. To overcome this issue, simplified models allowing the identification of regular dynamics structures have been introduced.

Among them, the Keplerian two-body model is generally used for preliminary research into the motion of artificial bodies in space. In fact its straightforward mathematical formulation and tested closed form solution makes it the simplest choice. However, modern astrodynamics frequently looks for feasible solutions in complex non-Keplerian systems in order to improve the trajectory design capabilities and dynamical models predictions. Of great interest is the case of three masses, the so called Three-Body Problem. Despite

the reduced number of attractors, no general closed-form solution can still be found. But, assuming that one of the three bodies has a negligible gravitational attraction and that the two other massive bodies orbit around each other according to Kepler rules, the search for periodic and quasi-periodic solutions can be greatly enhanced. These assumptions define the so-called Restricted 3-Body Problem (R3BP), that will be analyzed in the next subsection.

2.1.1. Circular Restricted 3-Body Problem

The CR3BP describes the dynamics of a small body subjected to the gravitational attraction of two main bodies, called primaries, which are moving on a circular trajectory around their Center of Mass (CoM). The third mass does not affect the motion of the other two since it is considered negligible. Generally, the problem is represented in a not inertial rotating frame, as depicted in Figure 2.1, so that the primaries appear stationary. The adopted three dimensional frame $[\hat{x}, \hat{y}, \hat{z}]$ has origin in the center of mass of the system, with $\hat{x}$-axis corresponding to the primaries conjunction line, $\hat{z}$-axis perpendicular to the plane containing them and $\hat{y}$-axis following the right-hand rule. In this way, the two main bodies are located respectively on the $\hat{x}$-axis at the points $(-\mu, 0)$ and $(1-\mu, 0)$.

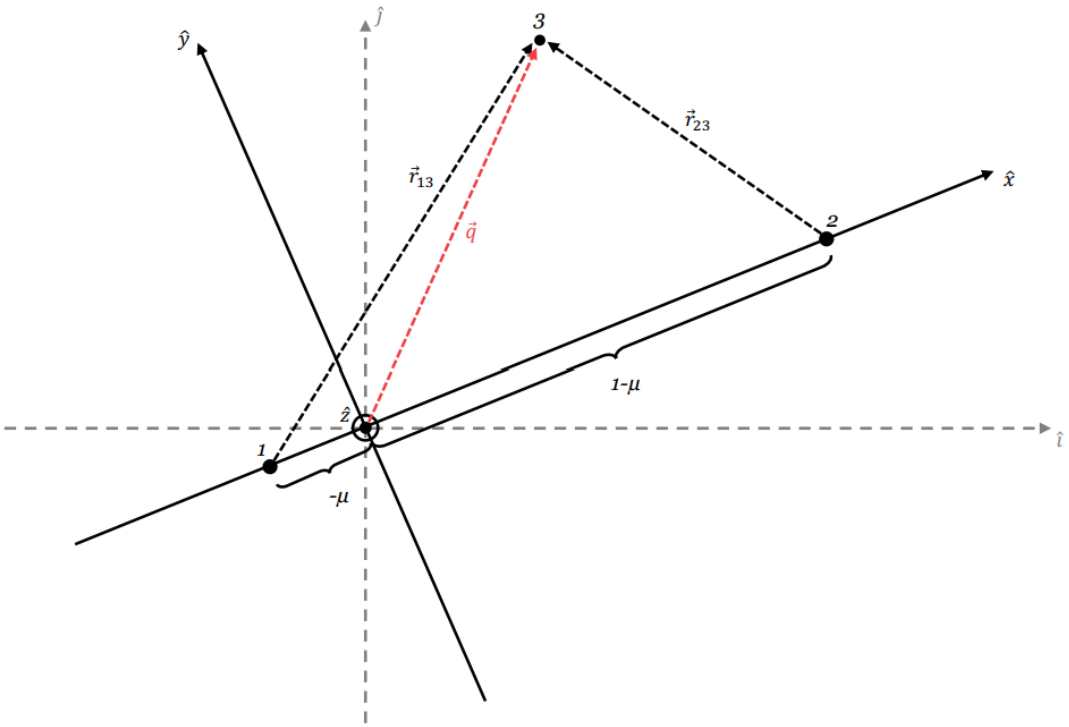

Figure 2.1: CR3BP model

The attractors distance, total mass, time, and angular velocity are commonly expressed in a non-dimensional form in CR3BP equations of motion. In particular, the masses of the bodies are normalized by the mass of the Sun-Earth system, leading to the non dimensional parameter μ:

$$\mu = \frac{M_E}{M_S + M_E} = 3.0404 \times 10^{-6} \tag{2.2}$$

where M_E is the Earth mass and M_S is the Sun mass. Length d, velocity v and time t are instead normalized as reported in the following expression.

$$\begin{cases} d' = Ld \\ t' = \frac{T}{2\pi} t \\ v' = Vv \end{cases} \tag{2.3}$$

It can be noticed that the primed quantities are dimensional and related to the non-primed non-dimensional quantities through the unitary quantities reported in Table 2.1.

L [km]	T [days]	V $[\frac{km}{s}]$
149.6×10^6	365.25	4.74

Table 2.1: Adimensionalization quantities

Thus, the non-dimensional equations of motion, in the synodic frame, read:

$$\begin{cases} \ddot{x} - 2\dot{y} = \mathcal{U}_x \\ \ddot{y} + 2\dot{x} = \mathcal{U}_y \\ \ddot{z} = \mathcal{U}_z \end{cases} \tag{2.4}$$

where the pseudo-potential $\mathcal{U}$ function, combining the gravitational potential of two primary bodies into a single effective potential, is defined as:

$$\mathcal{U}^{(\mathrm{CR3BP})} = \frac{1}{2}\left(x^2 + y^2\right) + \frac{1-\mu}{r_{13}} + \frac{\mu}{r_{23}} \tag{2.5}$$

In this formula, $\frac{1-\mu}{r_{13}}$ and $\frac{\mu}{r_{23}}$ terms represent the point mass gravitational potential of the two attractors, expressed in non-dimensional form, with r_{13} and r_{23} being the distances of the third body from the primaries.

The pseudo-potential function expressed in Equation 2.5 determines the motion of a test particle in the system. In particular, there are five specific positions in which the effective potential is stationary, and the net force acting on a test particle is zero. Therefore, a particle placed at one of these points, will remain stationary with respect to the two primary bodies. These points, called Lagrangian points (as they were discovered by Joseph-Louis Lagrange in 1772), are important in space mission planning, as they allow spacecrafts to remain in a stable position relative to the two primary bodies, without expending large amounts of fuel.

Their location can be determined analytically using the set of Equations 2.6. Three of the Lagrange points, denoted L1, L2, and L3 are collinear points and lie on the line connecting the two massive bodies, while the other two, denoted L4 and L5, form equilateral triangles with the two massive bodies [20].

$$\begin{cases} L_1 = (1-\mu, 0) \\ L_2 = (1+\mu, 0) \\ L_3 = (-\mu, \pm\sqrt{3}(1-\mu)) \\ L_4 = \left(\frac{1}{2} - \frac{1}{2}\sqrt{5}, \frac{1}{2}\sqrt{3}\right) \\ L_5 = \left(\frac{1}{2} + \frac{1}{2}\sqrt{5}, \frac{1}{2}\sqrt{3}\right) \end{cases} \tag{2.6}$$

Once the positions of the Lagrange points are known, they can be used to plan spacecraft trajectories and to study the stability of the three-body system. In addition, as it appears from the Equations of motion (EoM), the problem is autonomous since it is not directly related to the independent variable t. This implies that infinite periodic and quasi-periodic trajectories may be identified and developed continuously in families as described in the following sections.

2.1.2. Periodic orbits

As mentioned in Chapter 1, this work will present a performance analysis for different orbital configurations with the TSC placed on a reference periodic orbit and the OSC on a toroidal quasi periodic orbit around it.

The following sections deal with two classes of reference orbits in the 3-Body environment, representing possible planar and out-of-plane candidates for the studied mission.

- **Planar Lyapunov Orbits**. Closed trajectories lying in the x-y plane. They are symmetrical with respect to the x-z plane and do not have out-of-plane oscillations. They are bounded in the proximity of L1 or L2 and are unstable. This means that with no correction in position and velocity the satellite naturally leaves the trajectory on an unstable manifold.

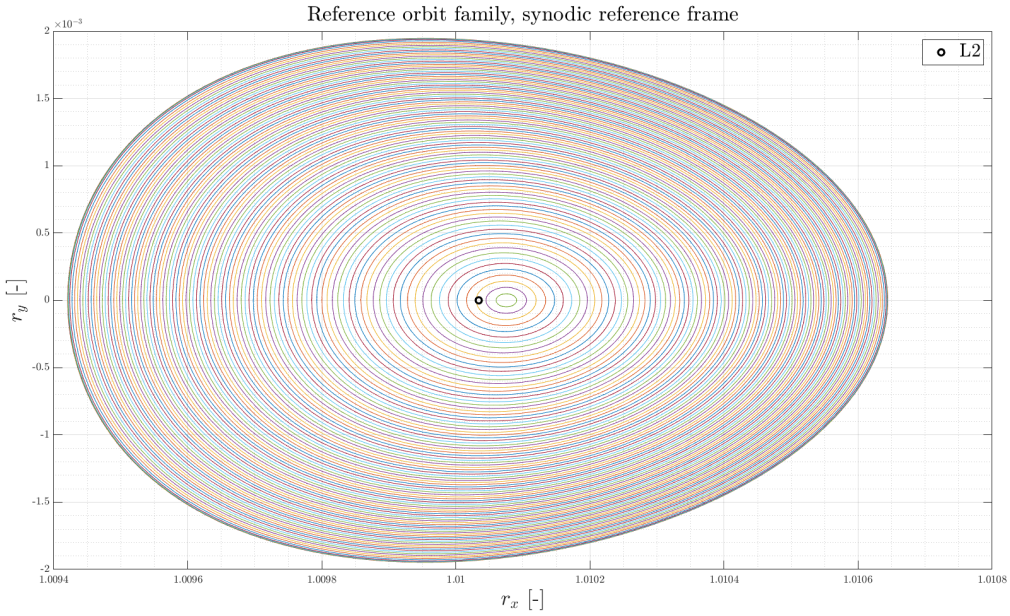

Figure 2.2: Lyapunov orbit family

- **Halo Orbits**. Closed trajectories with both in-plane and out-of-plane components. They are symmetrical with respect to the x-z plane and, like the Lyapunov, are unstable. These trajectories can be found with shooting methods starting from an initial solution and zeroing the desired objective function.

Regardless the orbit class, the most promising alternative foresees operative orbits around L2 Lagrangian equilibrium point in Sun-Earth system. This choice led to some useful

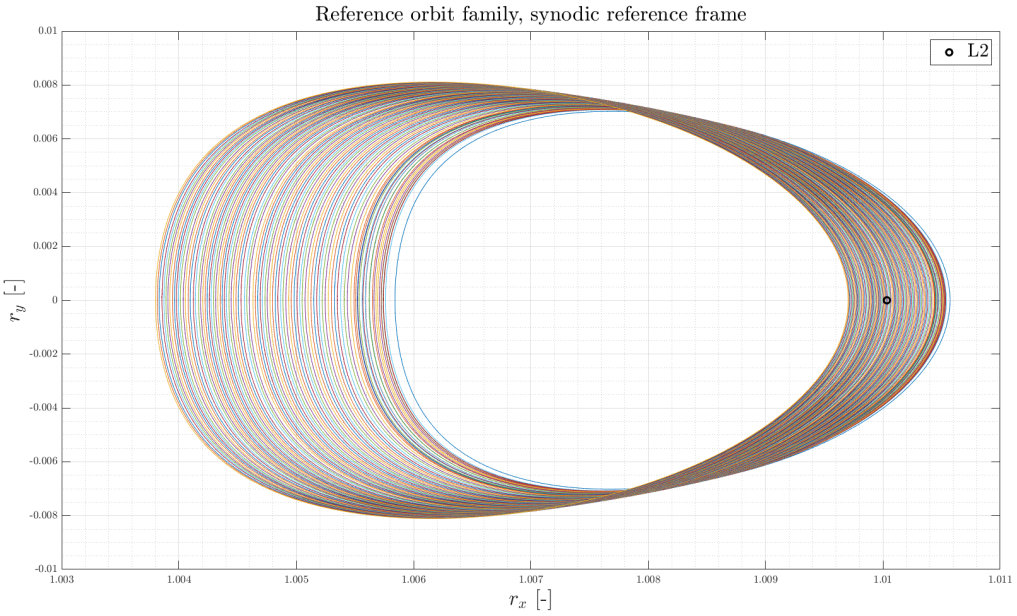

Figure 2.3: Halo orbit family

advantages. Firstly, L2 is an ideal location for exoplanet observation as it provides a stable environment with a clear view of the sky, and it allows for continuous observation without interruptions due to eclipses or Earth occultation. In fact, eclipses are ruled out orbiting along such a trajectory, since Earth shadow cone is never met. Constance of solar exposition together with large orbit and long period enable to provide a long duration observation for the selected star. Secondly, these orbits provide a way to maintain the formation in a precise and stable way without requiring constant adjustments to the spacecraft position. These orbits are periodic but not exactly circular, and they repeat over time, allowing the spacecraft to stay in a fixed region of space without the need for constant propulsion. This is particularly important for formation flying as it reduces fuel consumption and simplifies the control of the spacecrafts. Additionally, quasi-periodic orbits around L2 provide a wide range of possible distances between the Telescope and the Occulter, allowing for flexibility in the design of the system and the optimization of the performances. Moreover, orbital perturbations are very small, just correlated with SRP and 3-Body effect, with the result of a very stable dynamics, very appealing condition for a flying cluster operating in a very tight formation. Finally, absence of a relevant radiation source, such as Van Allen belts for an Earth orbit, avoids constant and periodic radiation bursts to the electronics and sensitive components on-board. Cosmic Rays are the only radiation source in this kind of environment.

Halo Periodic Orbits Generation

The generation of periodic Halo orbits has been performed using the Richardson third-order analytical approximation. The method consists in solving the equations of motion for a spacecraft in the vicinity of collinear Lagrange points in the restricted three-body problem, linearize them, and express their solution as combinations of sine and cosine functions with fixed frequencies.

To obtain periodic halo orbits, the amplitudes of the in-plane and out-of-plane motions must be of sufficient magnitude, so that the non-linear contributions to the system produce eigenfrequencies that are equal. This can be expressed mathematically by constraining the amplitudes and phases of the in-plane and out-of-plane motions using a certain non-linear algebraic relationship found as a result of the application of the perturbation method. The complete approach is shown in [21], here only the final third-order solution for periodic motion is reported.

$$\begin{cases} x = a_{21}A_x^2 + a_{22}A_z^2 - A_x\cos\tau_1 + (a_{23}A_x^2 - a_{24}A_z^2)\cos 2\tau_1 + (a_{31}A_x^3 - a_{32}A_xA_z^2)\cos 3\tau_1 \\ \\ y = kA_x\sin\tau_1 + (b_{21}A_x^2 - b_{22}A_z^2)\sin 2\tau_1 + (b_{31}A_x^3 - b_{32}A_xA_z^2)\sin 3\tau_1 \\ \\ z = \delta_n A_z\cos\tau_1 + \delta_n d_{21}A_xA_z(\cos 2\tau_1 - 3) + \delta_n(d_{32}A_zA_x^2 - d_{31}A_z^3)\cos 3\tau_1 \end{cases} \tag{2.7}$$

These method is essential for generating halo orbits, which are highly useful for space missions, such as orbiting communication satellites or conducting scientific observations from stable platforms, as the case of exoplanets observation mission.

Lyapunov Periodic Orbits Generation

Lyapunov periodic orbits are a type of periodic orbits that exists in the vicinity of unstable equilibria in dynamical systems. They can be generated starting from an initial guess in the Lagrangian point L2 center manifold. This guess should be a set of initial conditions that satisfies the equations of motion in the L2 frame. Let this initial guess be denoted as x_0. The initial guess is then propagated forward in time using a numerical integrator,

such as Runge-Kutta. This will return a trajectory in the L2 frame, denoted as $x(t)$.

At this point the deviation vector between the trajectory and the L2 center manifold is computed. This is the vector that connects the trajectory to the manifold at each point in time. Let this deviation vector be denoted as $\xi(t)$.

$$\xi(t) = \mathbf{x(t)} - \mathbf{x_m}(t) \tag{2.8}$$

where $x(t)$ is the trajectory at time t, $x_m(t)$ is the point on the L2 center manifold that is closest to $x(t)$, and $\xi(t)$ is the deviation vector at time t.

Variational equations along the trajectory can be now evaluated. These equations describe the evolution of the deviation vector over time. The variational equations can be expressed as:

$$\frac{d\delta\xi}{dt} = \mathbf{A}(t)\delta\xi \tag{2.9}$$

where $A(t)$ is the Jacobian of the equations of motion with respect to the deviation vector evaluated along the trajectory, and $\delta\xi$ is the variation of the deviation vector.

The variational equations are used to construct a linear map that takes the deviation vector from one point in time to the next. This linear map is given by the matrix exponential of $A(t)$ that takes the deviation vector from time t_0 to time t.

$$\phi(t, t_0) = \exp\left[\int_{t_0}^{t} \mathbf{A}(\tau)d\tau\right] \tag{2.10}$$

Compute the eigenvalues and eigenvectors of the linear map $\boldsymbol{\phi}(t, t_0)$. The eigenvectors correspond to the directions in which the deviation vector grows or shrinks, while the eigenvalues indicate the rate of growth or decay. Let λ_1, λ_2, and λ_3 be the eigenvalues of $\phi(t, t_0)$ and let ν_1, ν_2, and ν_3 be the corresponding eigenvectors.

Choose an eigenvector corresponding to a growth rate of unity. This eigenvector corre-

sponds to the direction in which the deviation vector grows at a constant rate. Let this eigenvector be denoted as ν_1.

Use this eigenvector ν_1 as the initial guess for a new periodic orbit in the L2 center manifold. Repeat the steps until the periodic orbit converges to a Lyapunov periodic orbit.

The key idea behind this method is to use the variational equations to identify the direction in which the deviation vector grows at a constant rate, and then use this direction to refine the initial guess for the periodic orbit. By iteratively repeating this process, we can converge to a Lyapunov periodic orbit.

2.1.3. Quasi-Periodic orbits

The specific focus of this thesis is on the performance analysis of Quasi-Periodic Orbital Families for exoplanet observation using Telescope-Occulter Formation Flying. Quasi-periodic orbits are those that repeat themselves with some variation over a long period of time. This analysis is crucial to understand the stability and feasibility of this approach for exoplanets observation.

One of the main advantages of using Quasi-Periodic Orbital Families for this purpose is that it allows a more efficient use of resources. QPOFs are a set of periodic, non-resonant trajectories that have been identified in the CR3BP. These trajectories can be used by spacecrafts to achieve stable and repeatable formation flying, which is critical for the success of Star-shade based exoplanet imaging missions. By using QPOFs, spacecraft can fly in formation for longer periods of time, which can result in longer observation windows and a higher probability of successfully detecting exoplanets. Additionally, QPOFs can be designed to avoid certain regions of the sky that may interfere with observations, such as bright stars or the Sun. This can improve the overall performance of the observation mission and increase the chances of discovering Earth-like exoplanets.

So, Quasi-Periodic Orbital structures are developed to enable a natural, bounded relative motion between the agents of the Formation, minimizing the control effort and frequency for the maintenance. In fact quasi-periodic orbits around L2 are inherently stable, which means that spacecrafts can remain in the same orbit for extended periods of time without requiring significant station-keeping maneuvers. This is particularly useful for long-duration observation missions.

In this work, a higher order continuation algorithm proposed in [22] for computing Quasi-Periodic orbits and their stability in the CR3BP has been followed. The proposed ap-

proach is based on the typical "Prediction-Correction", but it is efficiently designed to speed up the generation of full orbital families, thanks to improved prediction goodness and larger continuation steps. The overall scheme structure, depicted in Figure A.1, is divided into main parts, the initialization and the continuation loop.

Initialization. The initialization of the process consists in collecting the state **X** and period τ of the first two initial orbits, usually derived from classical schemes, in the vector $\boldsymbol{\chi}$.

$$\boldsymbol{\chi} = \begin{bmatrix} \boldsymbol{X} \\ \tau \end{bmatrix} \tag{2.11}$$

Continuation Loop. The Continuation Loop is based on the following steps.

1. Guess generation. A state guess is obtained using a particular polynomial approximation whose coefficients are evaluated starting from the linear system and the current curvilinear abscissa step (variable for polynomial prediction, see details in [22]).

2. Correction. The correction is performed in order to satisfy the constraint function $F(x)$ defined as:

$$\boldsymbol{F}_{,k,l} = \begin{bmatrix} \boldsymbol{\varphi}\left(\boldsymbol{X}_{,k,l}, \tau_{,k,l}\right) - \boldsymbol{X}_{,k,l} \\ \boldsymbol{\sigma}\left(\boldsymbol{\chi}_{,k,l}\right) \end{bmatrix} \tag{2.12}$$

   where $\boldsymbol{\varphi}\left(\boldsymbol{X}_{,k,l}, \tau_{,k,l}\right)$ is the propagation of the initial state for one orbital period while $\boldsymbol{X}_{,k,l}$ is the trajectory final condition. So, the first constraint of Equation 2.12 ensures periodicity after one orbit. The symbol $\boldsymbol{\sigma}\left(\boldsymbol{\chi}_{,k,l}\right)$ instead, represents the set of Poincaré phase conditions [23], specific for each orbital family.

3. Step Update. After obtaining the corrected state, checks on the goodness of the iteration are conducted. Specifically, the iteration is deemed acceptable only when two conditions are met: firstly, the correction must be effective, which means that the residual should be lower than a specified tolerance level. Secondly, the prediction made by the initial guess should be sufficiently close to the final corrected

value. In case one or both conditions are not satisfied, the iteration is rejected, and the continuation step is modified to a lower and more conservative value. If both constraints are respected, the iteration is accepted, and the algorithm proceeds.

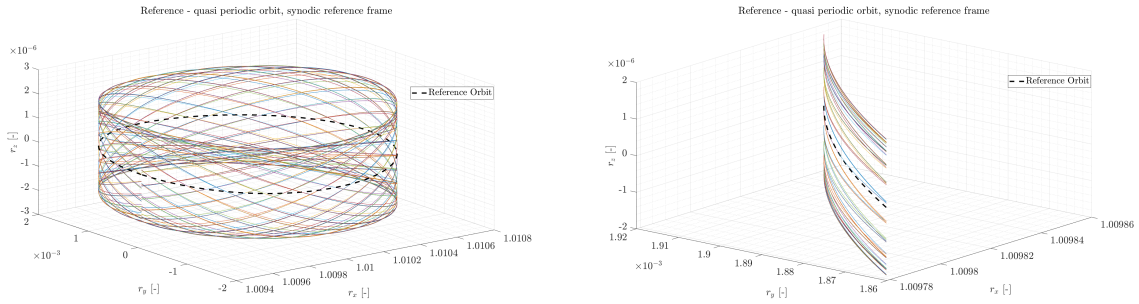

Figure 2.4: Quasi-periodic Lyapunov family (left) and zoomed view (right)

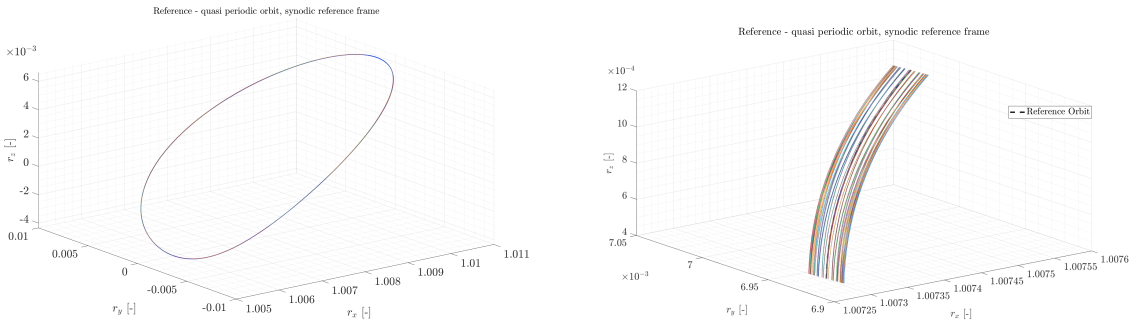

Figure 2.5: Quasi-periodic Halo family (left) and zoomed view (right)

2.1.4. Orbit-attitude CR3BP model

The analysis of the natural relative 6 Degree of Freedom (DoF) motion is carried out within the simplified framework of the CR3BP. It represents the simplest orbital model able to catch the main features of the attractive non-Keplerian multi-body Sun-Earth environment. The Euler rotation equations are included into the classical CR3BP dynamics, so that the orbit-attitude motion can be propagated simultaneously [24].

As mentioned in section 2.1.1 the CR3BP describes the motion of a spacecraft m, under the gravitational attraction of m_1 and m_2. The spacecraft is assumed as a rigid body, with negligible mass with respect to the primaries ($m \ll m_1, m_2$). Within CR3BP simplification, the primaries move on circular orbits about their common barycentre with constant angular velocity Ω_s. The study of the relative dynamics involves two independent spacecraft, which are labelled Telescope with mass m_{TSC}, and Occulter, with mass m_{OSC}.

The absolute orbital states $\mathbf{x}_{orb} = [\mathbf{r}, \mathbf{v}] = [x, y, z, v_x, v_y, v_z]$ describe the position and velocity of the center of mass of the two spacecraft, $\mathbf{x}_{orb,TSC}$ and $\mathbf{x}_{orb,OSC}$, which are expressed in the synodic rotating frame. The attitude quaternions $\mathbf{q}_{TSC}$ and $\mathbf{q}_{OSC}$ parametrize the orientation of the body-fixed frames with respect to the inertial frame. The body-fixed frames of the spacecraft, $\hat{\mathbf{b}}_{TSC} = \hat{\mathbf{t}}_1, \hat{\mathbf{t}}_2, \hat{\mathbf{t}}_3$ and $\hat{\mathbf{b}}_{OSC} = \hat{\mathbf{o}}_1, \hat{\mathbf{o}}_2, \hat{\mathbf{o}}_3$, are located at the center of mass of the corresponding spacecraft and they are aligned with their principal inertia directions. The angular rates, $\boldsymbol{\omega}_{TSC}$ and $\boldsymbol{\omega}_{OSC}$, relative to the inertial frame and expressed in the respective body-fixed frames, complete the attitude states of the spacecraft. All the equations involved are reported below.

The classical CR3BP dynamical equations:

$$\begin{cases} \dot{x} = v_x \\ \dot{y} = v_y \\ \dot{z} = v_z \\ \dot{v_x} = x + 2v_y - \frac{(1-\mu)(x+\mu)}{r_1^3} - \frac{\mu(x-1+\mu)}{r_2^3} \\ \dot{v_y} = y - 2v_x - \frac{(1-\mu)y}{r_1^3} - \frac{\mu y}{r_2^3} \\ \dot{v_z} = -\frac{(1-\mu)z}{r_1^3} - \frac{\mu z}{r_2^3} \end{cases} \tag{2.13}$$

where r_1 and r_2 are the distances of the generic spacecraft from the first and second primary, respectively, and μ is the mass ratio of the two primaries.

The Euler equations of rotational dynamics:

$$\begin{cases} \dot{\omega_1} = \frac{I_3 - I_2}{I_1} \left[3(1-\mu)\frac{g_2}{r_1^5} + \frac{3\mu}{r_2^5}(h_2 h_3 - \omega_2 \omega_3) \right] + \alpha_{1,SRP} + \alpha_{1,control} \\ \dot{\omega_2} = \frac{I_1 - I_3}{I_2} \left[3(1-\mu)\frac{g_1}{r_1^5} + \frac{3\mu}{r_2^5}(h_1 h_3 - \omega_1 \omega_3) \right] + \alpha_{2,SRP} + \alpha_{2,control} \\ \dot{\omega_3} = \frac{I_2 - I_1}{I_3} \left[3(1-\mu)\frac{g_1}{r_1^5} + \frac{3\mu}{r_2^5}(h_1 h_2 - \omega_1 \omega_2) \right] + \alpha_{3,SRP} + \alpha_{3,control} \end{cases} \tag{2.14}$$

where $I = \text{diag}[I_1, I_2, I_3]$ is the inertia matrix of the generic spacecraft aligned to its principal inertia axes, g_i and h_i are the direction cosines of the radial vector going from the i-th primary to the spacecraft expressed in the body-fixed frame.

The quaternion kinematic equations read:

$$\begin{cases} \dot{q}_1 = \frac{1}{2}(\omega_3 q_2 - \omega_2 q_3 + \omega_1 q_4) \\ \dot{q}_2 = \frac{1}{2}(-\omega_3 q_1 + \omega_1 q_3 + \omega_2 q_4) \\ \dot{q}_3 = \frac{1}{2}(\omega_2 q_1 - \omega_1 q_2 + \omega_3 q_4) \\ \dot{q}_4 = \frac{1}{2}(-\omega_1 q_1 - \omega_2 q_2 - \omega_3 q_3) \end{cases} \tag{2.15}$$

where q_1, q_2, q_3, q_4 are the quaternion components and ω_1, ω_2, ω_3 are the angular velocity components. Quaternions normalization has to be ensured according to Equation 2.16 to avoid numerical instabilities.

$$q_1^2 + q_2^2 + q_3^2 + q_4^2 = 1 \tag{2.16}$$

The system of differential equations can be summarized as:

$$\begin{cases} \dot{\mathbf{x}}_{\mathbf{orb}} = f_{CR3BP}(\mathbf{x}_{\mathbf{orb}}) \\ \dot{\mathbf{q}} = f_q(\mathbf{q}, \boldsymbol{\omega}) \\ \dot{\boldsymbol{\omega}} = f_\omega(\mathbf{x}_{\mathbf{orb}}, \mathbf{q}, \boldsymbol{\omega}) \end{cases} \tag{2.17}$$

where x_{orb} is the state vector of the spacecraft in the circular restricted three-body problem (CR3BP), f_{CR3BP} is the CR3BP dynamics function, q is the attitude quaternion, ω is the angular velocity, f_q is the quaternion kinematic equations, and f_ω is the angular velocity dynamics function.

2.1.5. Perturbations: Solar Radiation Pressure

The Solar Radiation Pressure (SRP) is one of the largest perturbations experienced by an object, especially in non-Keplerian trajectories of the Sun-Earth system far from the attractors. It is defined as the pressure generated by an photon flux from the Sun hitting a surface of the spacecraft [25]. Since the incoming radiation carries momentum and energy, the interaction with a generic body generates a dynamical perturbation. For a classical spacecraft, the SRP contribution is few orders of magnitude smaller than the gravity gradient torques generated by the two primaries. However, its effect should not be neglected to run accurate simulations, because cumulative effect could influence the spacecraft dynamics over long periods.

$$P_{SRP} = \frac{\phi_{SRP}}{c} \tag{2.18}$$

In this formula $c = 299792458\ m/s$ is the speed of light, and ϕ_{SRP} is the flux density (power per unit surface) of solar radiation at the distance of the body from the Sun, approximately of 1350 W/m^2.

Assuming that the incident radiation can be absorbed, specularly reflected and in part diffusely reflected, three coefficients are introduced to indicate those fractions of the incident flux, respectively ρ_a, ρ_r and ρ_d. Their sum is constrained to equal unity according to Equation 2.19, since no energy can be lost before and after the interaction. In this work they are assumed to have typical values for space-graded materials.

$$\rho_a + \rho_r + \rho_d = 1 \tag{2.19}$$

At this point, the radiation force can be modeled assuming that the surfaces of the spacecraft are flat panels. The $i-th$ force due to solar radiation pressure is described:

$$\mathbf{F_{SRP_i}} = -PA_i(\hat{s_b} \cdot \hat{n_{bi}})[(1-\rho_s)\hat{s_b} + (2\rho_s(\hat{s_b} \cdot \hat{n_{bi}}) + \frac{2}{3}\rho_d)\hat{n_{bi}})] \tag{2.20}$$

where $\hat{s_b}$ indicates the Sun direction, $\hat{n_{bi}}$ the normal to the A_i surface of the spacecraft.

If the $i-th$ spacecraft surface is pointing towards the Sun with a positive incident angle, meaning that the dot product between $\hat{s_b}$ and $\hat{n_{bi}}$ directions is greater than zero, then the torque T_{SRP} is calculated according to Equation 2.21, otherwise it is null.

$$\begin{cases} \mathbf{M_{SRP}} = \sum_{i=1}^{n} r_i \times F_{SRP_i} \quad if \ \ \hat{n}_{b_i} \cdot \hat{s}_b > 0 \\ \mathbf{M_{SRP}} = 0 \quad if \ \ \hat{n}_{b_i} \cdot \hat{s}_b < 0 \end{cases} \tag{2.21}$$

3 | Mission Design

The Star-shade technology is a promising concept for exoplanet observatory design. It cleanly resolves issues that have arisen over the last decade and provides a viable solution for direct spectroscopy. In fact, by using direct spectroscopy, we can learn about the chemical composition and other key properties of exoplanet atmospheres, but with the Star-shade, we can accomplish this without requiring ultra-high wave front quality correction and maintenance for the Telescope. By fully suppressing the starlight before it enters the Telescope, we can focus on studying the light from the exoplanet and gaining a deeper understanding of our universe. In this chapter different aspects of mission design will be presented.

3.1. Mission geometry

The external Occulter, or Star-shade, is an opaque screen that is flown into the LoS between the Telescope and the star being observed. As represented in Figure 3.1, if the Star-shade is positioned sufficiently far, it will subtend a small angle and can block out the light from the star, while allowing the light from an exoplanet to pass over the edge unobstructed. It should be pointed out that the Occulter must be larger in diameter than the aperture of the Telescope and must be positioned enough far away to cast a sufficient shadow to fully darken the Telescope aperture. For example, a Star-shade that is at least 5 meters in diameter can subtend a 0.2 arcsecond angle and be positioned 5 million kilometers away. Thus, the Star-shade mission concept requires two spacecrafts flying at large separations.

However, in order to obtain the mentioned configuration geometry, high precision is required to perform the correct Formation Flying alignment. In fact, the Telescope shall maintain a range baseline b from the occulting Star-shade, while the Occulter is held in the LoS from the Telescope to the target. The Telescope pointing error θ_{err}, is stringent, but it represents a well-known problem in Telescope attitude control and so it will not be discussed further in this work. The alignment error, offset of the Occulter from the Telescope focal line, should be ideally zero. Finally, the Inner Working Angle (IWA) is a critical parameter for exoplanet observation missions since it directly affects the sensi-

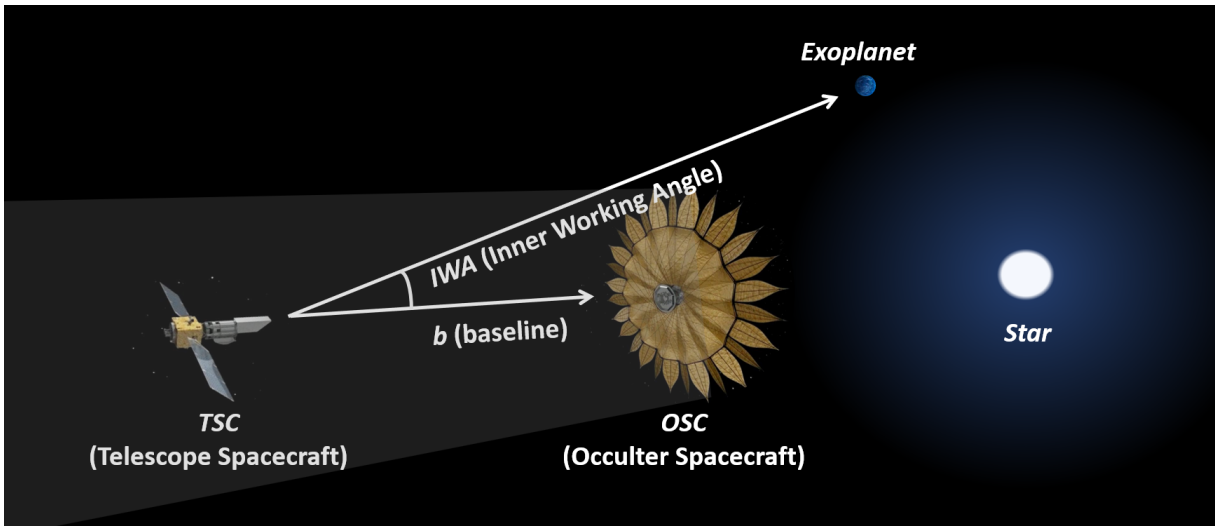

Figure 3.1: TSC- OSC configuration geometry

tivity and resolution of the imaging system. It describes the minimum angular distance between the host star and the observed exoplanet that can be resolved by the imaging system. These parameters will be deeply investigated in the next sections.

3.1.1. Telescope - Occulter Baseline

As anticipated in Chapter 1, an external Occulter is therefore an opaque screen that is placed in front of a Telescope for high-contrast imaging. Its purpose is to eliminate most of the light from a bright stellar object before it ever reaches the Telescope, so that objects near the light source are not overwhelmed by stray light from scattering and aberrations in the Telescope optics. Occulters were first proposed for solar coronagraphy in 1948 [26], and for finding extrasolar planets in 1962 [1]. However, while recent Occulters designed for solar coronagraphy fly detached from the spacecraft at a distance on the order of 100 m [27], Star-shade aimed at extra-solar planet searches, such as those proposed in [28] and [29] are located tens or hundreds of thousands of kilometers away. Only these distances allow objects within 1 *mas* or less to be imaged. In this section all the parameters influenced by Telescope - Occulter baseline will be presented.

The distance between the star and the observer, d_{star}, and the Telescope-Occulter distance b, are related through the basic geometry of the problem, as follows:

$$\frac{d_{star}}{b} = \frac{\alpha_{occ}}{\alpha_{star}} \tag{3.1}$$

where α_{occ} is the angular size of the Occulter and α_{star} is the angular size of the star as seen from the observer. In order to achieve the desired level of contrast between the star and any potential exoplanets, the Occulter must block out as much of the starlight as possible, which requires a large Occulter size relative to the star size. However, the distance between the Occulter and the Telescope must also be large enough to create a shadow that fully covers the Telescope aperture, which requires a smaller Occulter size relative to the distance between the star and the observer. These competing factors must be carefully balanced in order to optimize the performance of the instrument and achieve the desired scientific goals.

3.1.2. Occulter Area

Another critical factor in the design of an external Occulter mission is the area of the Occulter. Being the approximated Occulter area A_{Occ} equal to

$$A_{Occ} = \pi \ (R_{Occ})^2 \tag{3.2}$$

It can be related to the Occulter-Telescope distance b, through Equation 3.3.

$$R_{Occ} = b \ \tan(IWA) \tag{3.3}$$

where R_{occ} is the radius of the Occulter and IWA expresses the angular size of the star as seen from the Occulter. The area of the Occulter is a critical factor in determining the level of contrast that can be achieved between the star and any potential exoplanets, as well as the overall sensitivity and performance of the instrument. Larger Occulters can block out more starlight and achieve higher contrast, but they also require longer TSC - OSC distances and may be more difficult to manufacture and deploy. Thus, optimizing the area of the Occulter is a critical trade-off that must be carefully considered in the design of an external Occulter mission.

Figure 3.2 shows the variation of baseline and Occulter area, as a function of different $IWAs$. It is interesting to notice that in order to achieve smaller separations, e.g. 0.5 mas, the Formation with a 1 m Occulter radius should reach baselines in the order of 10^4 km.

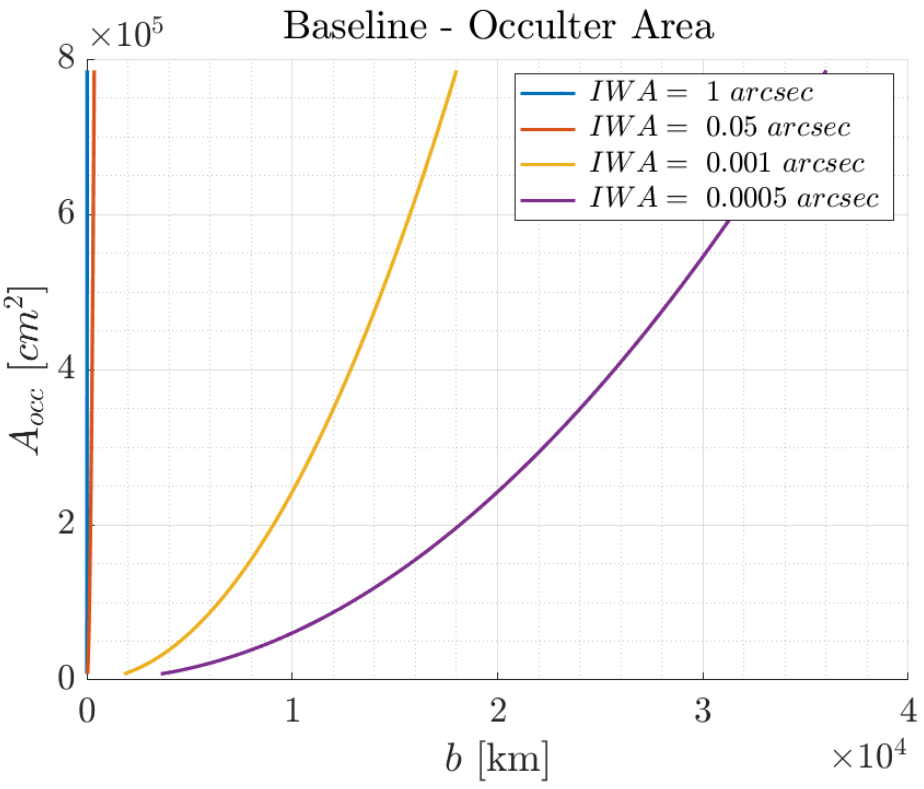

Figure 3.2: Baseline - Area Occulter for different IWA

3.2. Occulter spacecraft design

This section presents the constraints which are the basis for the Occulter design. For semplicity, the analysis is divided into two different parts, respectively the geometric considerations determined by the required size of the Occulter and shadow, and the engineering ones limiting realizable Occulter geometries.

3.2.1. Geometric Occulter design

To establish the design envelope based on geometric factors, refer to the model depicted in Figure 3.3. The figure illustrates the variables involved in the study, including the Occulter radius R_{Occ}, the baseline distance between spacecraft b, the allowed deviation from the baseline before shadow performance deteriorates beyond acceptable levels Δb, the radius of the shadow that is deep enough to enable scientific observations ρ. IWA is deeply discussed in Section 3.1 and λ denotes the wavelength of light. Note that the analysis is repeated for different wavelengths spanning from UV to Far-IR. The Fresnel number f is equivalent to the half-wavelength path length difference between the center and edge of the Occulter to the center of the Telescope. It is important to highlight

that some of these variables are not independent. Specifically, there are two constraints governing the relationship between R_{Occ}, b, f and λ. The constraint for IWA is given by the already mentioned Equation 3.3, while the equation for the Fresnel number according to Goodman [30] is:

$$f = \frac{R^2}{\lambda} \tag{3.4}$$

It can be seen that large values for Fresnel number are obtained in the ultraviolet spectrum. Thus, it would appear that using an ultraviolet Telescope would allow complete recovery of optical performance. However, there are two challenges to this approach. First, conventional mirror performance sharply degrades for wavelengths below 150 nm. Second, most stars have a very small fraction of their luminous output in the ultraviolet spectrum. Consequently, the ultraviolet flux from interesting targets will be very low, resulting in long integration times. Increasing the maximum wavelength of the science instrument will increase the available flux, but decrease the achievable Occulter contrast. It is therefore clear that the ideal Occulter for imaging a specified target depends on the emission spectrum of the target and the required contrast.

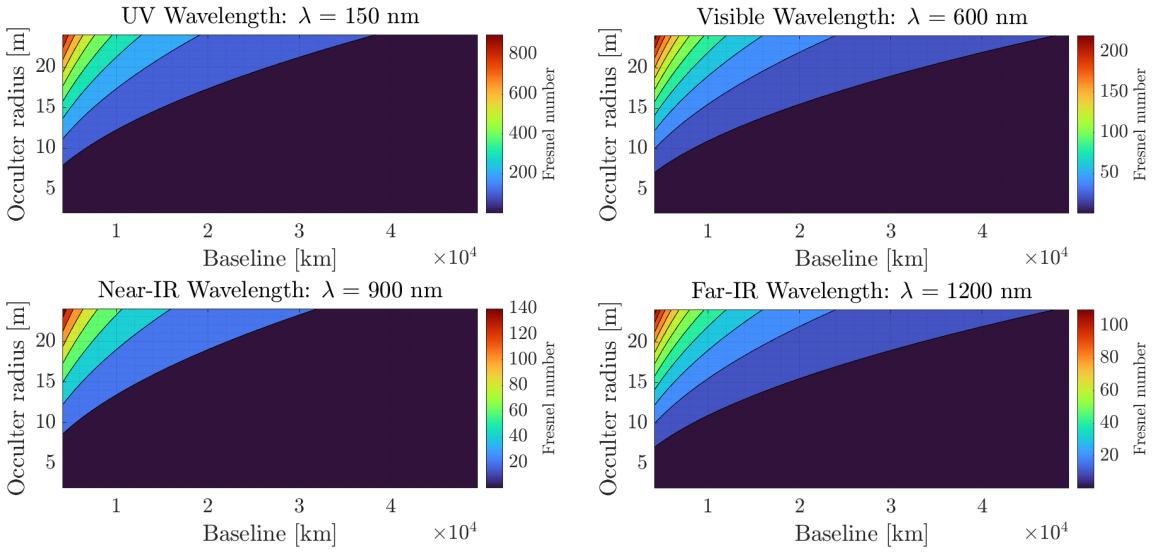

Figure 3.3: Occulter radius - Baseline - Fresnel number relation at different wavelengths

The choice of Fresnel number for a space Telescope using an external Occulter method to detect exoplanets depends on several factors, such as the size of the Occulter, the Telescope aperture, the observing wavelength, and the desired IWA. In general, a higher Fresnel number is preferred because it indicates that the diffraction effects are negligible

and the system behaves as if it was in free space. However, achieving a high Fresnel number can be challenging because it requires a large Occulter and a small separation distance between the Telescope and the Occulter itself. As a rough guideline, a Fresnel number of at least 10 (or more) is desirable for an external Occulter coronagraph to achieve good performance.

It is also worth mentioning that smaller wavelengths lead to a higher contrast ratio. However, from Figure 3.4 it is evident that only large enough Occulter areas are able to achieve the minimum scientifically relevant contrast of 10^{-10}.

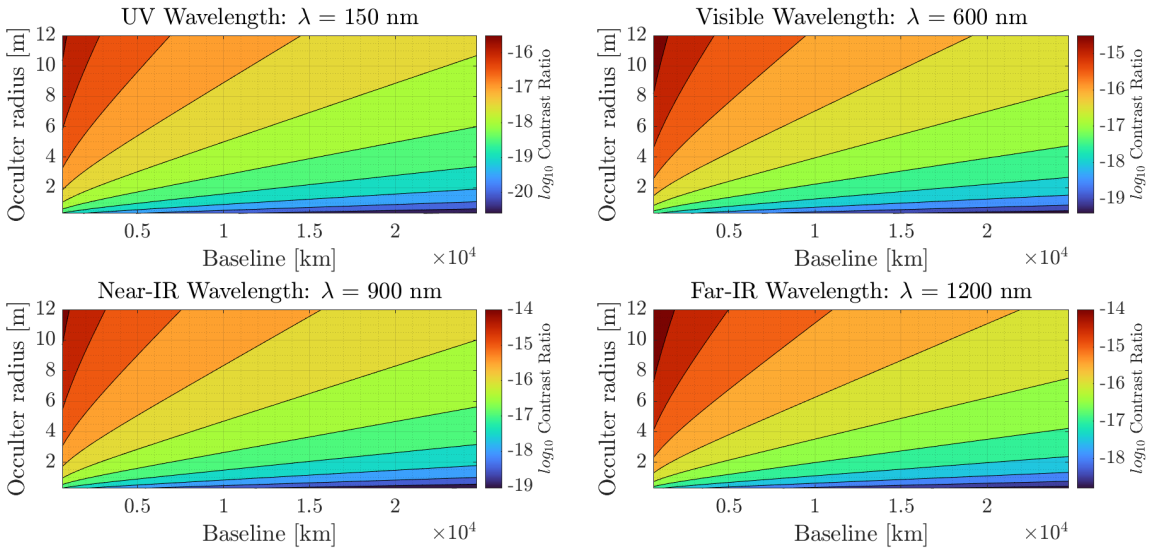

Figure 3.4: Occulter radius - Baseline - Contrast ratio relation at different wavelengths

3.2.2. Engineering Occulter design

Occulters are gaining increasing interest as a tool for achieving high-contrast for Earth-like planet imaging. However, the design of the Star-shade surface is one of the most crucial points determining the success of the mission. In fact, its primary function is to block the light of the parent star, which is significantly brighter than the planet under observation.

While a circular Occulter is a simple and straightforward design, it suffers from several disadvantages. One significant issue is the diffraction pattern that results from the wave nature of light passing through a circular aperture, known as the Airy pattern [31]. The diffraction pattern disperses the star light over a wider area, reducing the contrast between the planet and the star. Furthermore, circular Occulters have limited capacity to control the amount of starlight that leaks around their edges, further reducing contrast.

In contrast, petal-shaped Occulters, as the one represented in Figure 3.5 offer several advantages over circular ones. Petal-shaped Occulters are designed to reduce the diffraction pattern and, thus, increase the contrast between the planet and the star. The petals are precisely shaped and arranged to interfere destructively with the Airy pattern. This results in a significantly narrower diffraction pattern, which in turn enhances the contrast and increases the instrument sensitivity.

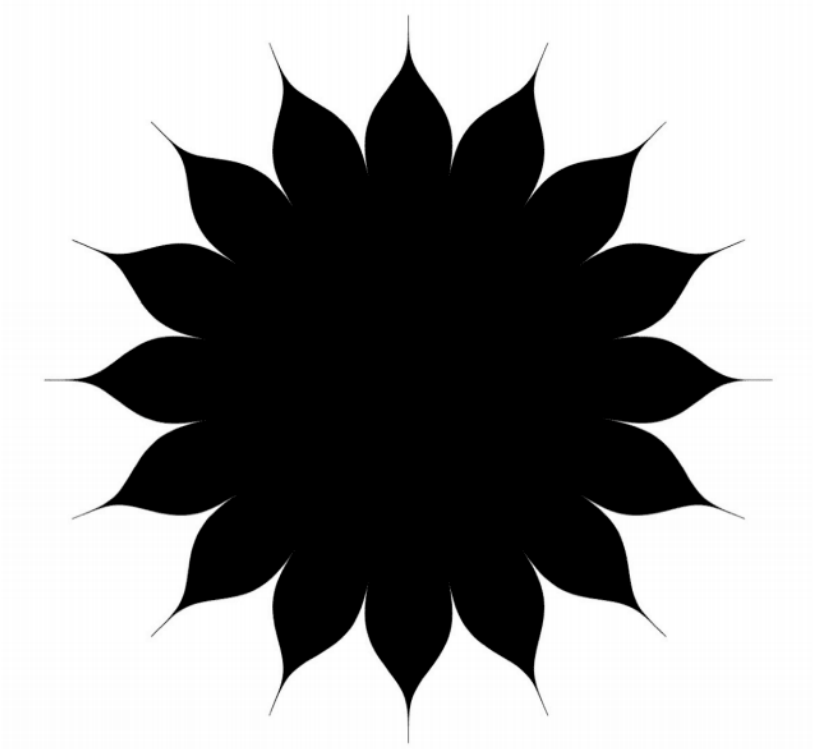

Figure 3.5: Petal-shaped Occulter

Petal-shaped Occulters also offer better control over the amount of starlight that leaks around the Occulter edges. Petals can be shaped, oriented, and sized to adjust the amount of leakage, depending on the Telescope size and the light wavelength. The effectiveness of this shape from the optical point of view is related to the number of petals: 12 is the minimum required to be effective, while from 16 onwards it follows an asymptotic trend [16]. For this work, attitude performance analysis will be therefore conducted with a sixteen-petals Star-shade.

The petal geometry is described by an apodization function $A(r)$ which denotes the fraction of the arc at radius r covered by the petal [28]. The relationship between the apodization function and the resulting petal geometry is illustrated in Figure 3.6 where θ is the angle subtended by the petal and $A(r)$ θ is the fraction of this angle covered by the petal.

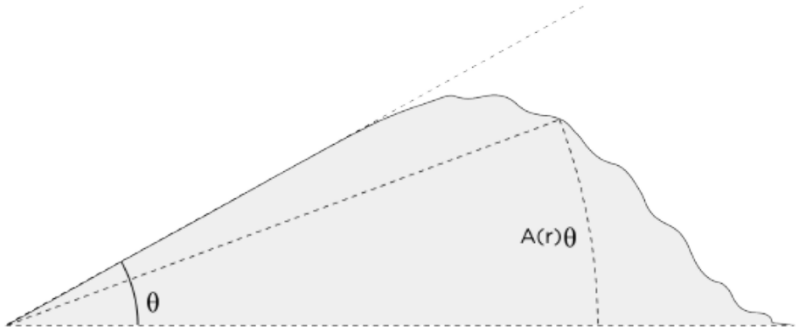

Figure 3.6: Apodization function petal geometry

Some geometric constraints shall be satisfied in order to ensure that the occulter is physically realizable. In particular, the second equation states that the occulter apodization function shall decrease monotonically in order to ensure structurally robust petal shapes. The third constraint specifies that the apodization function must be sufficiently smooth to allow the geometry to be precisely manufactured. If it is assumed that the occulter is machined with a 1 mm diameter bit, it is necessary that the maximum curvature of the occulter geometry, $c_{\max}$, be less than the curvature of the bit. The curvature of the occulter with a specified apodization profile depends on the number of petals, N.

$$\begin{cases} A(r) = 1 \quad r < R_{\text{solid}} \\ \frac{dA}{dr}(r) \leq 0 \quad 0 \leq r \leq R \\ \frac{\pi r}{N} \left| \frac{d^2 A}{dr^2}(r) \right| \leq c_{\max} \quad 0 \leq r \leq R \end{cases} \tag{3.5}$$

Manufacturing petals, together with the deployment of the Star-shade itself represent the major bottlenecks of the Occulter design. It has been shown that it is possible to build an Occulter petal to the stringent shape requirements for a terrestrial planet finding mission. For example, in the TDEM project [32] has been demonstrated the ability to manufacture a petal to flight-like processes and measure the shape with enough precision to meet mission milestone requirements.

3.3. Target selection

This section will delve into the scientific requirements that must be fulfilled by an exploration mission utilizing the coronagraph method with an external Occulter, to effectively

detect exoplanets within the habitable zone and search for potential signs of life. By thoroughly analyzing these requirements, we can compile a list of potential targets that are compatible with the mission capabilities.

Exoplanet Semi-Major Axis

Differently from other detection techniques, the coronagraph method is mainly used to detect exoplanets that are close to their host stars, typically within a few Astronomical Units (0.01 - 0.1 AU). This is because it relies on the ability to block the light emitted from the main star in order to identify clearly the exoplanets, that would be too faint to be observed if they were too far away. However, it is worth noting that this range is also dependent on the characteristics of the exoplanet (e.g. its size, mass, and albedo) as well as the properties of the host star, such as its luminosity.

Star Distance

The typical range of star distances can vary from a few to hundreds light-years, but it is not a strict limit and actual performance can depend on the specific instrumentation, observing conditions, and other factors.

Angular separation

The angular separation is a measure of the distance between two objects in the sky, as seen from an observer. The angular separation between the exoplanet and the host star can be calculated using the following formula:

$$\theta_{sep} = \frac{d_{Pl-S}}{d_S} \; 206265 \; [arcsec/pc] \tag{3.6}$$

Where d_{Pl-S} is the distance between the host star and exoplanet, which can be approximated to its orbit semi-major axis; while d_S is the star distance from the observer.

Contrast Ratio

The contrast ratio CR is defined as the ratio between the exoplanet F_Pl and its star fluxes F_S at the same wavelength. To detect Exo-Earth, the coronographic method needs to reach high CR, on the order of 10^{-10} [14] or lower.

$$CR\ (\lambda) = \frac{F_{Pl}}{F_S}\ (\lambda) \tag{3.7}$$

As anticipated, this parameter is also wavelength dependent and most of the exoplanet detection methods, including coronagraphic methods, observe in the near-infrared, where the exoplanets emit most of their thermal radiation. There are some simplified formulas that can be used to estimate the contrast ratio based on the properties of the exoplanet. One is to approximate the CR as the thermal flux ratio between star and exoplanet at a given wavelength. They are both assumed to be black body emitters in thermal equilibrium, in the absence of other sources of radiation or reflection.

In addition, CR is dependant on the specific instrumentation utilized on board. Equation 3.8 relates it with the Telescope diameter D_{Tel}.

$$D_{tel} = \sqrt{CR}\ \theta_{sep} \tag{3.8}$$

This formula assumes that the exoplanet is much fainter than the host star and that the main source of noise is the starlight that leaks through the coronagraphic mask. Other properties such as detector sensitivity and Telescope diffraction limitation are not taken into account. More detailed investigation shows in fact that CR is also affected by the residual speckles in the coronagraph caused by imperfections of the optical system, which are typically much brighter than the exoplanet signal so they need to be mitigated through advanced post-processing techniques.

Finally the CR at a given wavelength is also influenced by the host star spectral type. G-type stars, for example, are brighter at shorter wavelengths compared to K or M-type stars. Meaning that the contrast ratio between an exoplanet and a G-type star will be lower at shorter wavelengths than the same exoplanet orbiting a K or M-type star. Additionally, the presence of the exoplanet atmosphere absorbing starlight can change CR value significantly. In some cases, the contrast ratio can be improved at certain wavelengths where the exoplanet atmosphere is transparent and lets more light through.

Angular resolution

Angular resolution is a measure of the ability of an instrument or Telescope to distinguish small details in an image. It shall be considerably high in order to resolve the exoplanet from the host star with an external Occulter method. In general, the angular resolution (θ_{res}) can be expressed using the Raileight criterion:

$$\theta_{res} = 2.44 \, \frac{\lambda}{D_{tel}} \tag{3.9}$$

It should be pointed out that achieving high angular resolution also requires good stability and control over the optical system, and the use again of advanced post-processing techniques.

Signal to Noise Ratio

The signal-to-noise ratio (SNR) is a measure of the quality of an exoplanet observation, typically defined as the ratio of the exoplanet flux to the flux of the residual starlight leaking through the coronagraph. Higher SNR value indicates higher observation quality and a better chance of detecting and characterizing an exoplanet. The SNR required for an exoplanet observation mission with coronograph method depends on the specific requirements of the mission, such as the type of exoplanet being observed and the desired level of characterization. For example, for missions like TESS, the SNR is around $10-15$, while for missions like JWST the SNR is around $50-100$. The SNR is given by the formula:

$$SNR = \frac{F_{Pl}}{F_S} \, \frac{D_{tel}}{d_{Pl-S}} \, \sqrt{\frac{t_{exp}}{t_{int}}} \tag{3.10}$$

where t_{int} is the reference integration time, imposed equal to one day and t_{exp} is the exposure time of the observation.

Observation Time

A longer exposure time allows for more light to be collected, which can make it possible to detect fainter exoplanets. However, longer exposure times also increase the chances of

detector saturation, which can lead to image distortion. Therefore, the minimum period of observation should be chosen to balance the trade-off between collecting enough light and avoiding detector saturation and blurring. Generally it is taken at least equal to one planet period.

3.3.1. Mission Requirements

Table 3.1 summarizes all the scientific requirements to be satisfied for the mission design. In Figure 3.7 are shown all the possible exoplanets target observable by external Occulter method meeting the requirements.

a [AU]	**d_{Star} [pc]**	**θ_{sep} [arcsec]**	**CR [−]**	**D_{tel} [m]**	**θ_{res} [arcsec]**	**SNR [−]**	**T_{Obs} [days]**
0.01-0.1	0.05-50	0.0001-0.1	$\leq 10^{-9}$	0.3-10	$\leq \theta_{sep,MAX}$	> 10	$> T_{Orb}$

Table 3.1: Scientific requirements for exoplanet observation mission using coronograph method.

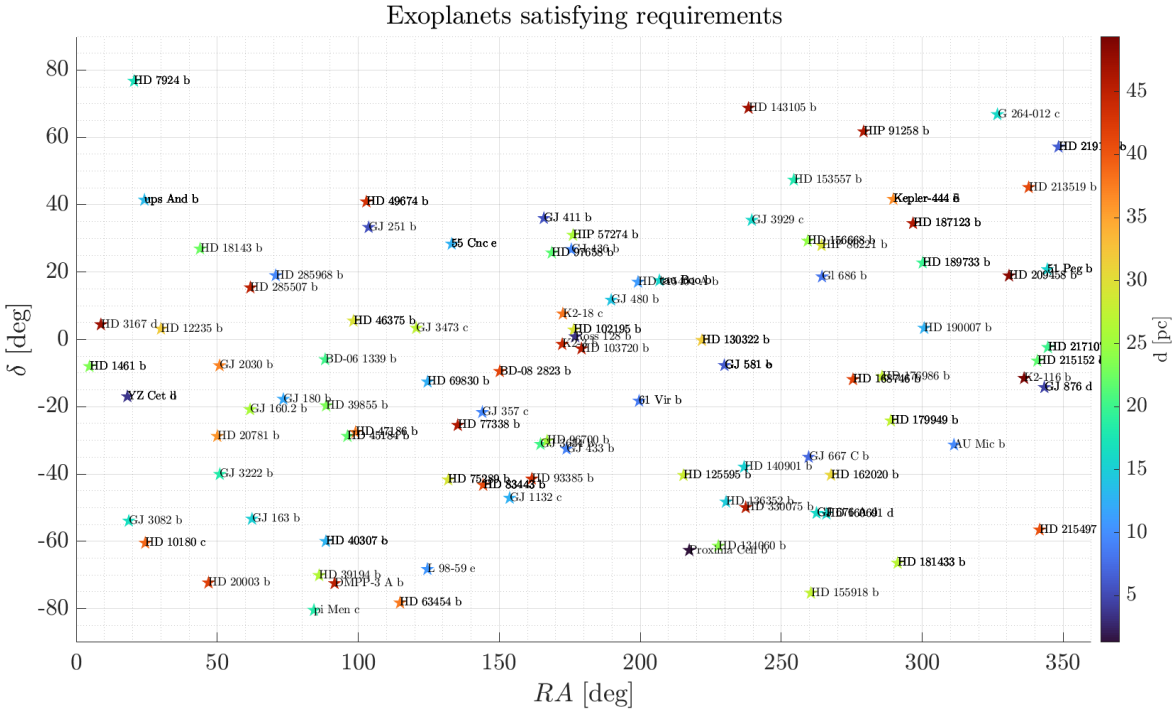

Figure 3.7: Observable Exoplanets with External Coronagraph method

4 | Performance Analysis

This chapter aims to investigate and compare the performances of various Telescope - Occulter orbital configurations for exoplanets observation. To evaluate the system behavior, several metrics such as target area, visibility time, and sky coverage are defined. Additionally, a phase shift is introduced between the reference and toroidal orbit. A comprehensive comparison between Halo and Lyapunov performances and the resulting optimal orbit configurations are presented. Furthermore, the chapter explores sub-optimal solutions by incorporating attitude dynamics into the problem. The optimization process provides the optimal control torque with SRP contribution to the EoM. Angular velocities of both Telescope and Occulter to ensure attitude stability are examined. The analysis assesses the acceptable relative pointing precision among the spacecrafts utilizing the proposed approach. The admissible values of pointing errors are documented with respect to the resultant degradation in the performances, in terms of CR and SNR. The chapter concludes with a table highlighting the major outcomes for both orbital families.

4.1. Performance definition

The optimization process conducted to find the best periodic and quasi - periodic couples starts with the definition of the desired target area to be observed and the performances involved in the study.

4.1.1. Target area

The choice of the observation region for this study was motivated by the high concentration of exoplanets found in the Galactic Center (GC). This was based on the information retrieved from Figure 4.1, showing all discovered and candidate exoplanets to date. The plot, generated starting from *NASA JPL Exoplanets Archive* [33], reveals a clear peak in the distribution of exoplanets in the galactic origin plane. Focusing the attention on this region provides an opportunity to increase the likelihood of finding exoplanets and to gain deeper insights into their distribution and formation within the galaxy. The desired target area is therefore defined as a cone-shaped region with a 10° aperture, centered in the GC.

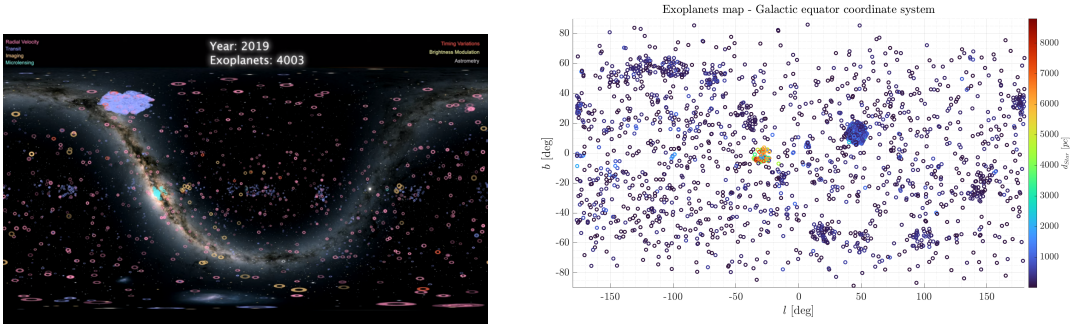

Figure 4.1: Exoplanet sky map: credits NASA (left), implemented map (right)

4.1.2. Orbital configurations definition

As anticipated, in section 2.1.2 the proposed orbital configurations foresee the placement of Telescope spacecraft and Occulter spacecraft respectively on a reference periodic orbit and a toroidal quasi - periodic orbit. However, for each Halo and planar Lyapunov reference orbit or element $n_{elements}$, there exists a number of tori $n_{toroids}$, around which the quasi periodic orbit is generated and several starting points n_{points}, from which such trajectory is initialized. All the possible combinations n_{total} analized are defined by the following relation:

$$n_{total} = {n_{elements}}^{{n_{toroids}}^{n_{points}}} \tag{4.1}$$

Still, in order to facilitate the identification of a single periodic quasi-periodic couple, two simple parameters are introduced. Each combination of these two trajectories can be determined by defining two orbital frequencies Ω_0, related to the periodic motion and Ω_1, which determines the quasi-periodic one.

However, since QPOFs are generated in a way such that both TSC and OSC trajectories start with the same azimuth angle, the baseline pointing direction between them would appear to be always around 90° with respect to the synodic plane, as can be seen for the Lyapunov - quasi Lyapunov example in Figure 4.2, thus limiting the region of observation.

From this reason comes the need of introducing an additional variable to the optimization problem. The chosen parameter is a shift s between the two spacecrafts, in order to increase the observation region visible with a specific configuration. Doing so, natural motion is exploited without necessarily controlling the orbital dynamics of the Telescope - Occulter Formation, again reducing mission costs.

Nevertheless, although the FF maintenance comes for free with the natural non - Keplerian

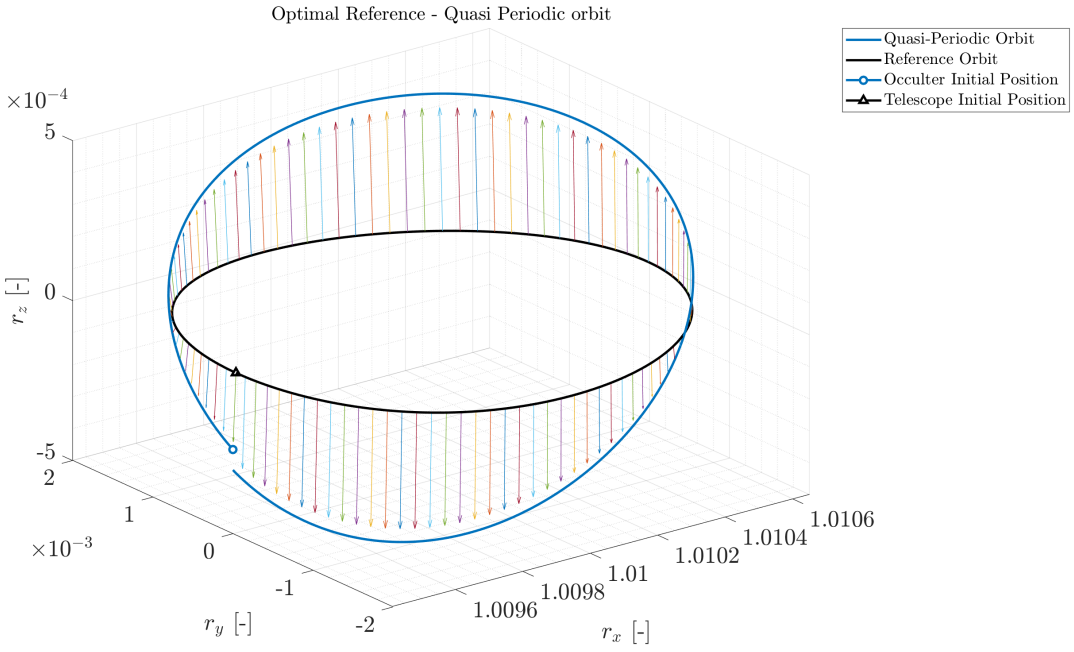

Figure 4.2: Telescope - Occulter baseline without shift

dynamics, as the name suggests, the quasi - periodic orbits do not perfectly close after one period. A small correction impulsive maneuver on the OSC is therefore required in order to repeat again the previous trajectory. The $\boldsymbol{\Delta_v}$ needed to maintain the Formation in the established orbital configuration is presented in the next sections. It is evaluated according to Equation 4.2, where $\mathbf{v_f}$ and $\mathbf{v_i}$ indicates the Occulter velocities at the end and at the beginning of the propagation respectively.

$$\boldsymbol{\Delta_v} = \mathbf{v}_f - \mathbf{v}_i \tag{4.2}$$

4.1.3. Sky Coverage

The sky coverage percentage A_{perc} is computed as the ratio of the total area of the sky covered by the space Telescope when in visibility of the target during the observation time to the total area of the observation region. For each time step, the portion of the sky covered by the space Telescope is computed as the area of a circle with a radius equal to the field of view (FOV) of the coarse camera. And the total area covered over time is evaluated by adding up the sky coverage for each time step, taking into account any overlap between consecutive time steps. The total area of the observation region is instead approximated as the product between the length and width of the observation

region, where the length is computed as the distance between two points separated by the maximum azimuth angle of the observation region (around 360°); while the width dimension is considered as the equivalent distance corresponding again to the camera FoV. The sky coverage percentage is therefore computed as:

$$A_{perc} = \frac{A_{vis}}{A_{total}} \cdot 100 \tag{4.3}$$

where A_{vis} is the total area of the sky covered by the space Telescope during the observation time, and A_{total} is the total area of the observation region.

4.1.4. Visibility Time

The visibility time percentage T_{perc} is computed as the ratio of the time during which the space Telescope is observing the region of interest to the total observation time T_{ref}, corresponding to the overall period of the orbit.

$$T_{perc} = \frac{T_{vis}}{T_{ref}} \cdot 100 \tag{4.4}$$

4.2. Performance analysis

In the previous sections, the methodology to built the FF orbital candidates has been defined. In the next paragraphs, the resulting performaces will be analyzed and compared for both the Halo and Lyapunov families.

4.2.1. Sky Coverage

Looking at the shape of the two orbital families, it can be clearly noticed that being the Lyapunov orbits planar, their baseline could ideally cover less region to be observed in the sky. On the contrary, being more inclined trajectories, the elevation vector of the LoS from the Telescope to the Occulter for the Halo orbits, span a broader observation area. Consequently, one would expect performances in terms of sky coverage for the Halo case to be higher than Lyapunov ones.

Figures 4.3 and 4.4 represent the percentage of area covered by all the different TSC - OSC orbital configurations, defined by the frequency parameters Ω_0 and Ω_1 and validates the predicted results. In fact, maximum performances are obtained for Halo orbital combinations with respect to Lyapunov ones. However, due to the introduction of a phase

shift between the Telescope and Occulter spacecrafts, a wider area of sky observation is achievable also with the Lyapunov family. This justifies the relatively small difference in the A_{perc} peaks for Halo 16.5% compared to 14.3% for the Lyapunov.

Another interesting point, that emerges from the plots, is the vertical pattern. In fact, for each Ω_0 - Ω_1 couple, 1000 different shifted configurations have been analyzed in terms of sky coverage. The Lyapunov orbits, due to their planar structure and the fact that the out-of-plane dimension is several orders of magnitude smaller than the in-plane ones, show an almost constant trend. In fact, where the graph appears empty, the evaluated A_{perc} is indeed equal to the maximum value for each possible shift angle, thus overlapping with each other.

The evolution for the other family is instead more variable. Nevertheless, there are some regions in the Halo plot, in which data are not available at all. This voids are caused by the fact that continuation method for quasi - periodic Halo generation has not produced orbits in certain regions, most probably where the non-Keplerian dynamics is more unstable.

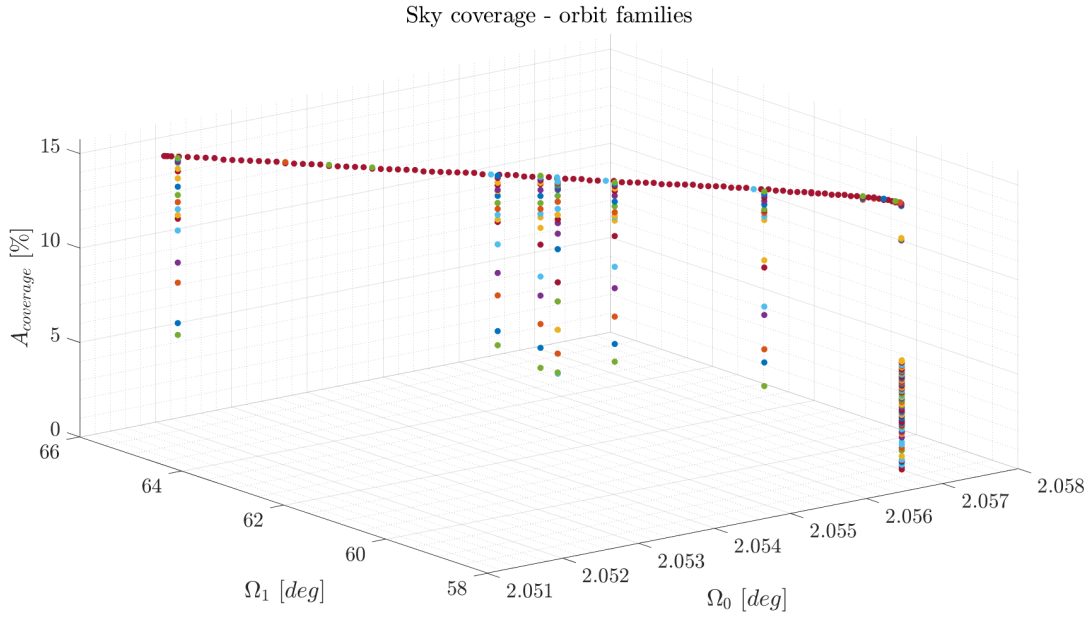

Figure 4.3: Lyapunov performances: Sky coverage

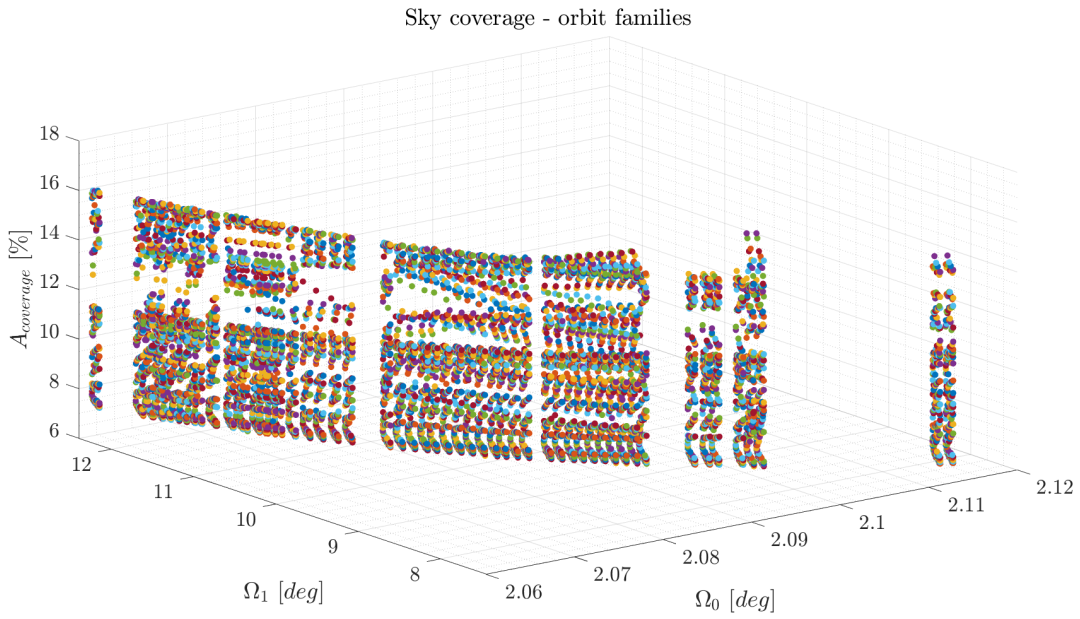

Figure 4.4: Halo performances: Sky coverage

4.2.2. Visibility Time

The same considerations hold true for the Visibility Time performance analysis. As a matter of fact, Figures 4.5 and 4.6 reveal the same scheme as before, but the discrepancy in the maximum value of T_{vis} is now more evident because of the different orbital periods of the two families. Halo orbits around L2 have indeed a period that oscillates between $160 - 200$ *days*, while Lyapunov orbits last about one year.

The problem has been constructed such that when the target is inside the camera FoV (10°), represented by green areas in Figures 4.7 and 4.8, visibility condition occurs. The plots confirm the previous results showing the star misalignment error $\theta_{err,star}$ with respect to the TSC - OSC formation, when no control torque is applied.

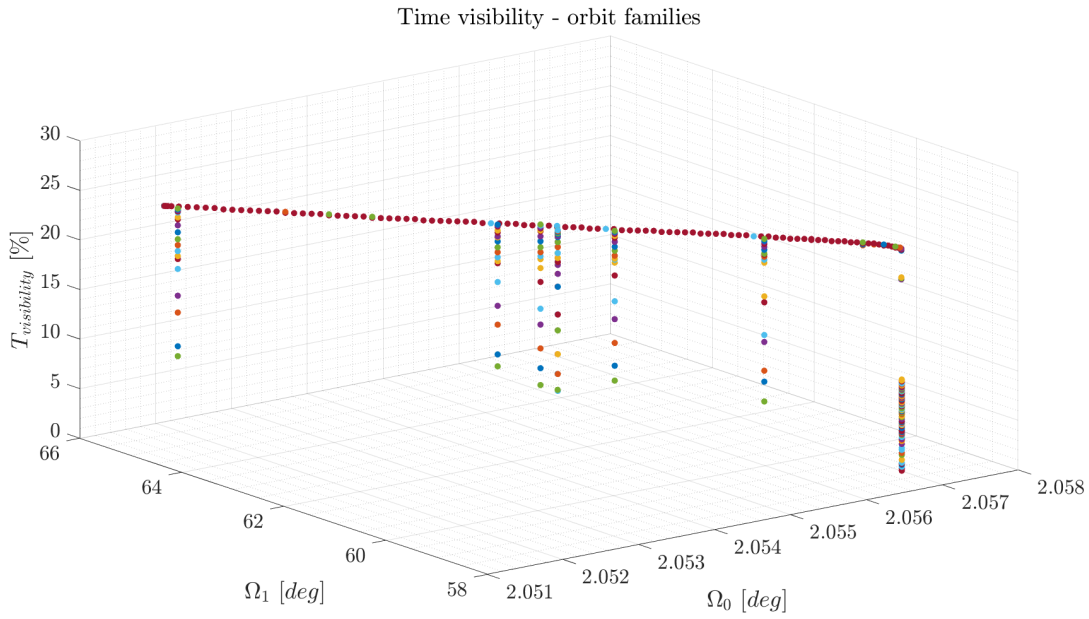

Figure 4.5: Lyapunov performances: Visibility Time

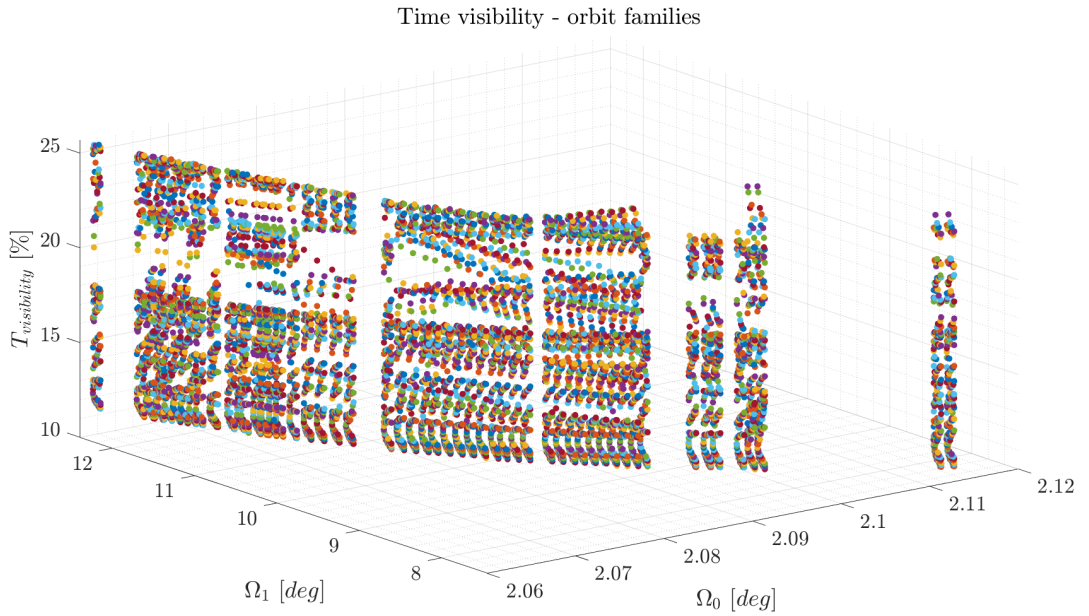

Figure 4.6: Halo performances: Visibility Time

4.3. Optimal Orbital configurations

In the following section, the optimal TSC - OSC orbital configurations are shown for both Halo and Lyapunov families. In particular, Table 4.4 reports the exact indexes and phase

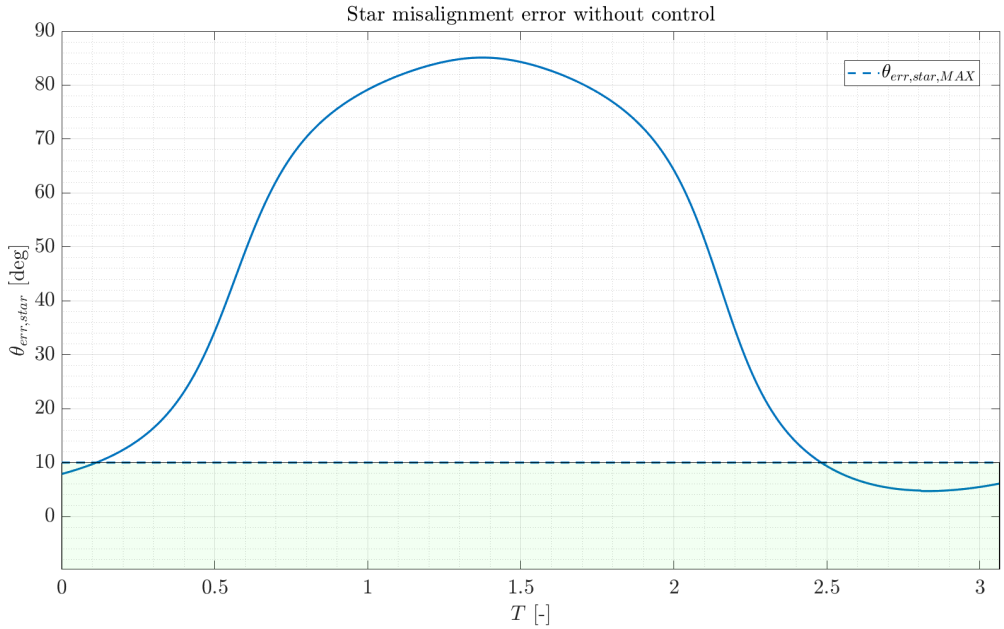

Figure 4.7: Lyapunov performances: Star misalignment error without attitude control.

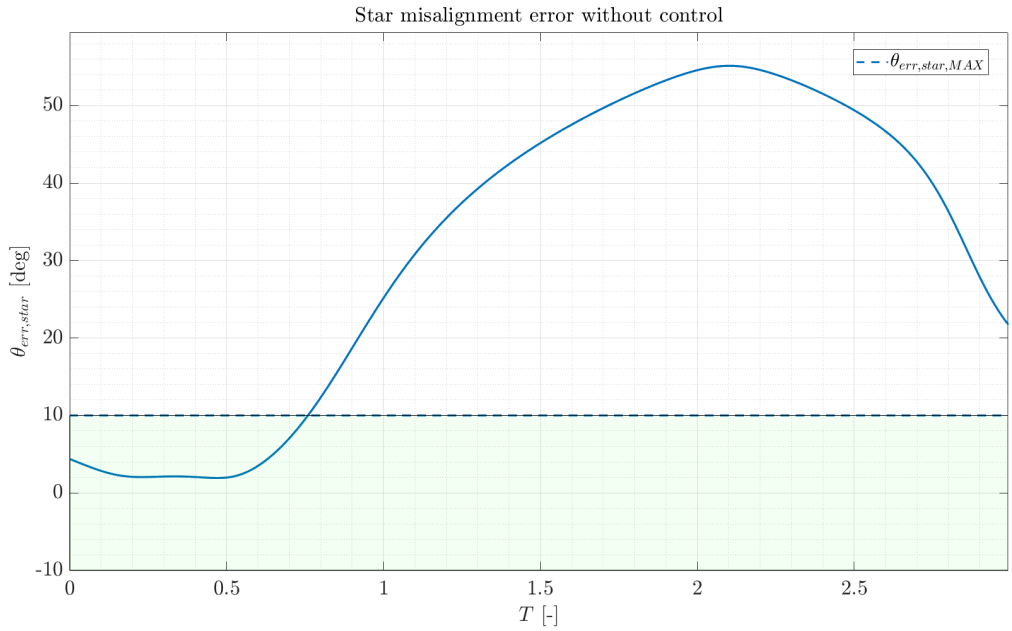

Figure 4.8: Halo performances: Star misalignment error without attitude control.

shifts, defined in Section 4.1.2, identifying the best reference and toroidal trajectories.

	Lyapunov	Halo
Ω_0	2.0513	2.0982
Ω_1	64.5792	8.2725
θ_{shift}	30.6°	0.72°

Table 4.1: Optimal Lyapunov and Halo configurations.

Figures 4.9 and 4.10 show the optimal periodic and quasi-periodic configurations for Lyapunov and Halo families that maximize the performances. In the legends the initial positions of Telescope and Occulter are reported. As anticipated from Table 4.4, the shift angle between the two spacecrafts assumes a greater value for the Lyapunov case. This is explained again by the fact that these orbits are planar, so in order for the baseline vector to be more sloped and cover a wider observation area, the shift angle should be significant. This does not happen for the Halo configuration, in which the optimal shift angle is 0.72° since these orbits are already inclined with respect to the Sun - Earth synodic reference system plane.

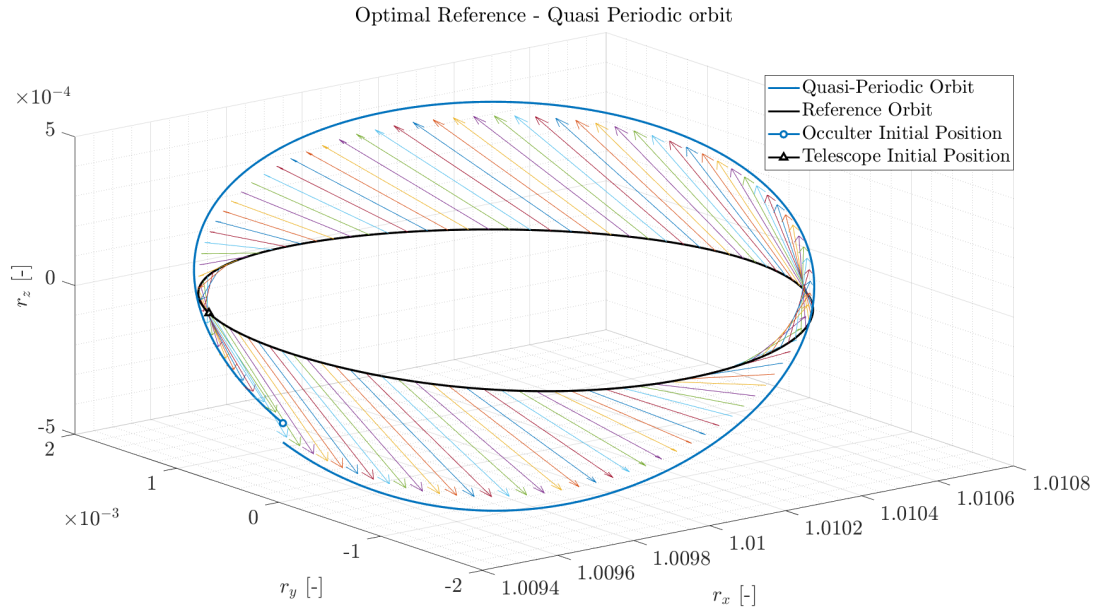

Figure 4.9: Optimal Periodic and Quasi-Periodic configuration for Lyapunov family

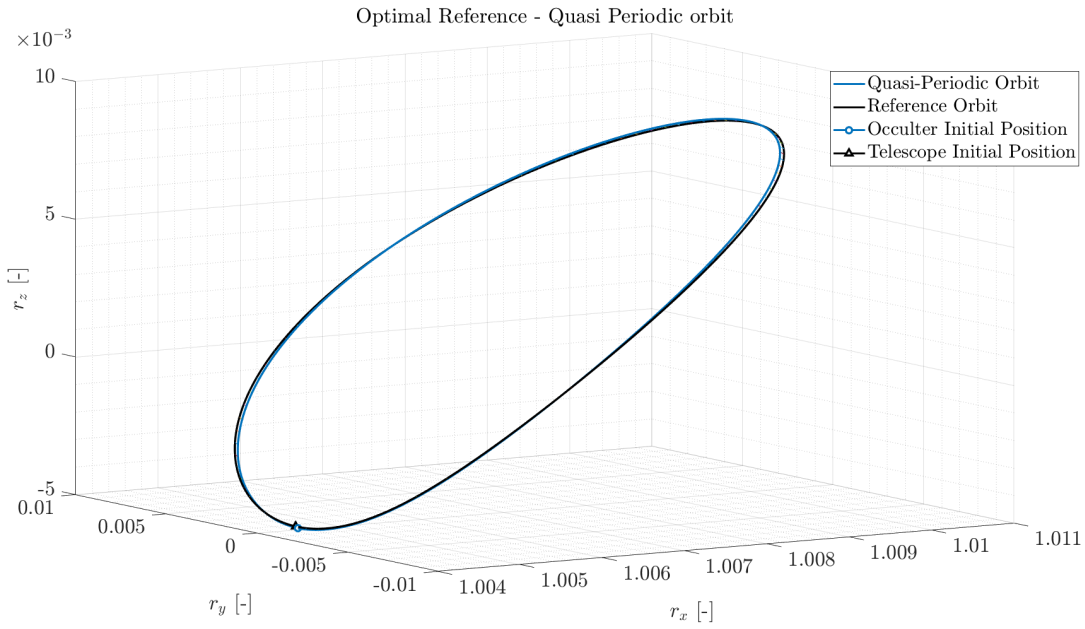

Figure 4.10: Optimal Periodic and Quasi-Periodic configuration for Halo family

In order to better visualize the motion of the Occulter spacecraft with respect to the Telescope, OSC relative trajectory around TSC (hence placed in the origin) has been printed for both the orbital families. From Figures 4.11 and 4.12 it clearly emerges that the quasi - periodic orbits do not close after one period, so a small $\boldsymbol{\Delta_v}$ correction on the OSC could be required. However, utilizing quasi-periodic orbits offers the significant advantage of being able to transition to another toroid without requiring additional propellant to return to the previous trajectory. This is achieved by means of a continuation method, which allows the spacecraft to smoothly move from one orbit to another, improving mission efficiency and flexibility.

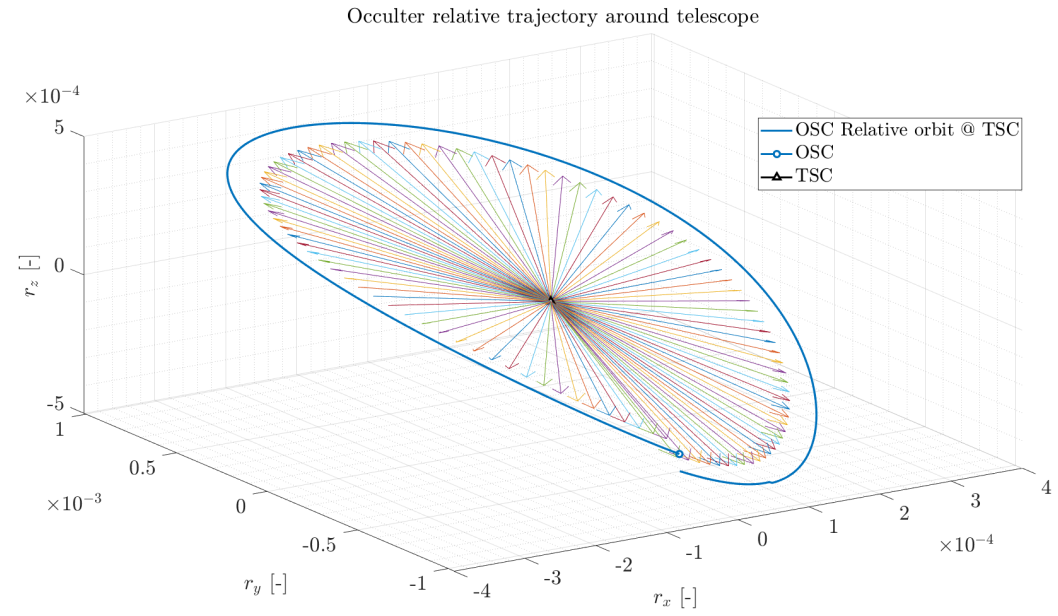

Figure 4.11: Occulter optimal relative trajectory around Telescope for Lyapunov family

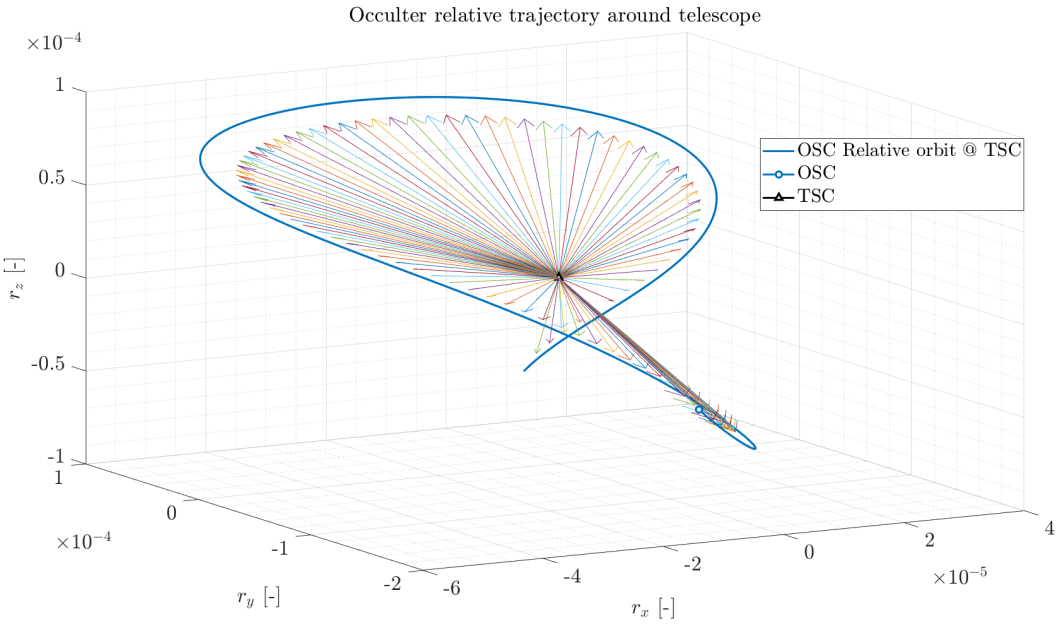

Figure 4.12: Occulter optimal relative trajectory around Telescope for Halo family

The following plots represent the baseline b variation over time between the two objects. It is worth mentioning that the values obtained for both Halo and planar Lyapunov families, in the order of $10^4 - 10^5$ km, are compatible with the numbers presented in the preliminary mission design in Chapter 3.

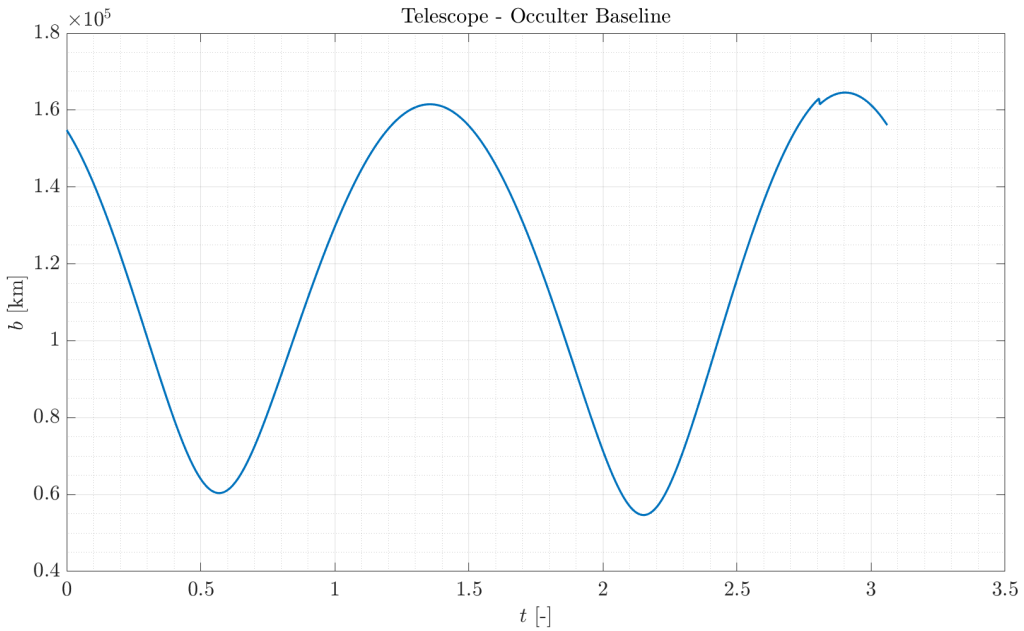

Figure 4.13: Telescope - Occulter baseline for Lyapunov optimal orbit

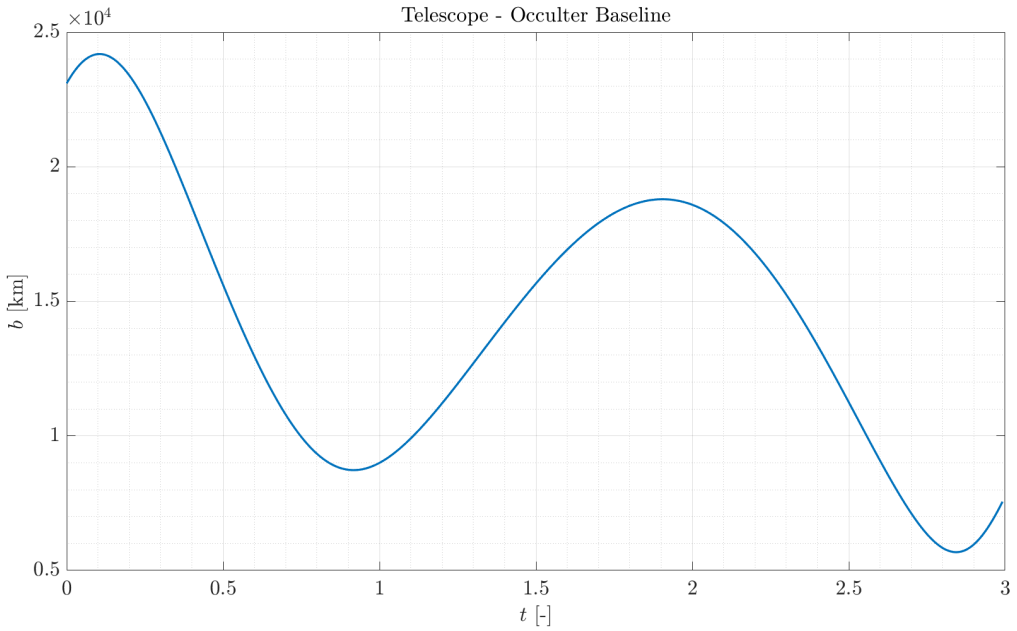

Figure 4.14: Telescope - Occulter baseline for Halo optimal orbit

Obtained the optimal orbital configurations and the corresponding baseline distances b for each QPOFs, the requirements for attitude analysis need to be assessed in terms of Inner Working Angle IWA and total pointing error θ_{err}.

It is important to recall that IWA can be calculated as $IWA = \frac{R_{Occ}}{b}$, where R_{Occ} is

the radius of the Occulter, that as it will explained in the next section, will be equal to 72.04 cm (A.3).

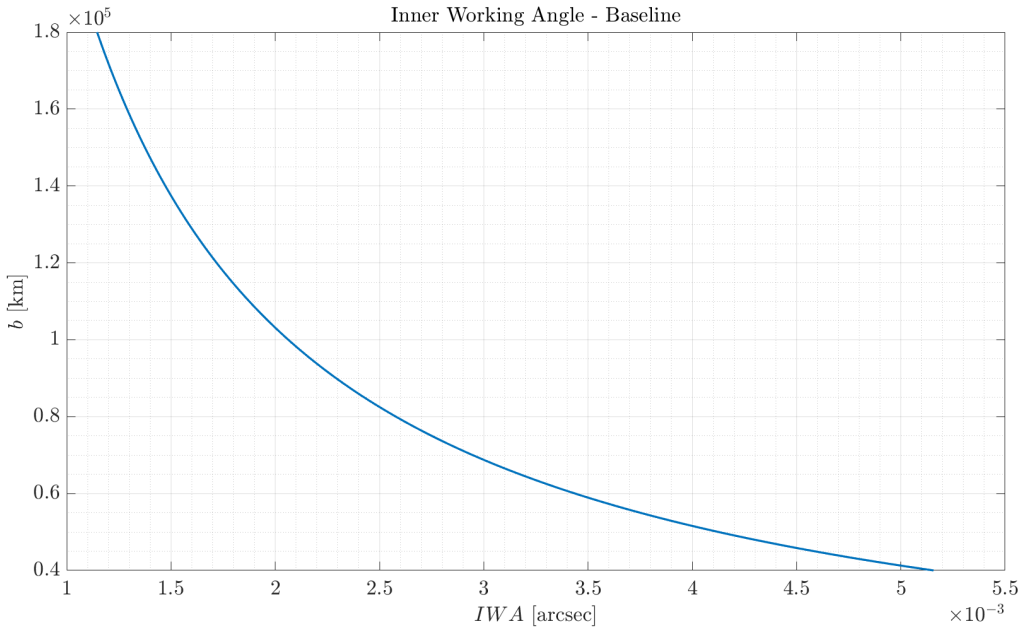

Figure 4.15: Lyapunov IWA - baseline relation.

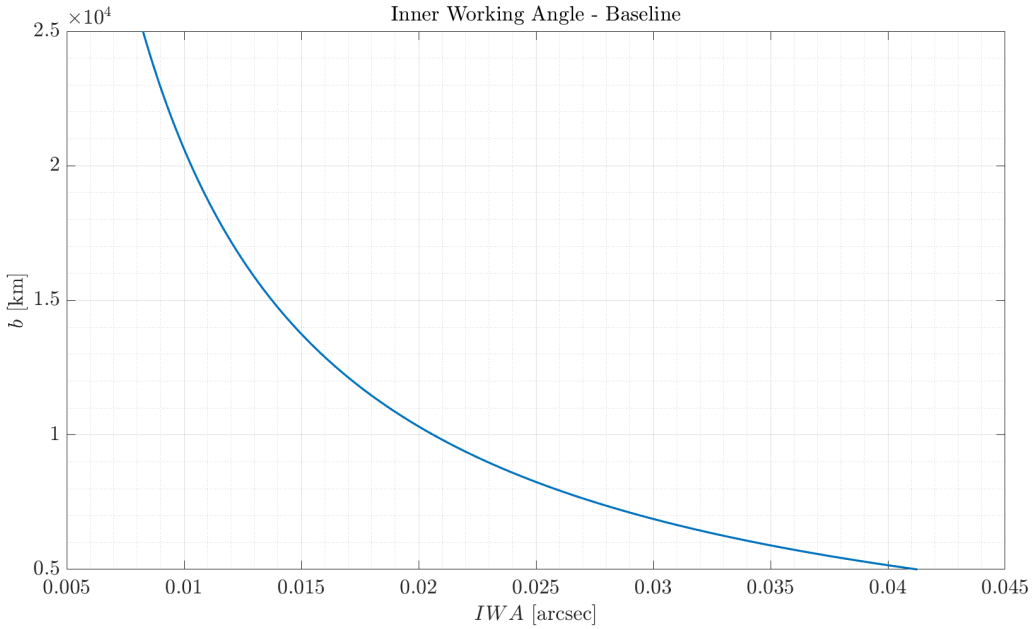

Figure 4.16: Halo IWA - Baseline relation.

Then, a maximum lateral offset L_{max} is set to be $< 30\%$ R_{Occ} because beyond this value the optical performances starts to degrade too much [19] affecting the quality of the

observation.

Fixed R_{Occ} and L_{max} values, Table 4.2 summarizes the attitude performance requirements calculated for both QPOFs. As visible from Figures 4.15 and 4.16, it is clear that pointing requirements for Lyapunov orbits are more demanding than Halo ones, since they deal with higher baseline ranges. These parameters will guide calculations in the next section.

	b	**IWA**	$\theta_{\mathbf{err}}$
Lyapunov	$\sim 10^5$ $[km]$	~ 0.005 $[arcsec]$	< 0.34 $[mas]$
Halo	$\sim 10^4$ $[km]$	~ 0.04 $[arcsec]$	< 2.5 $[mas]$

Table 4.2: Attitude Performance requirements.

4.4. Attitude TSC-OSC Scheme

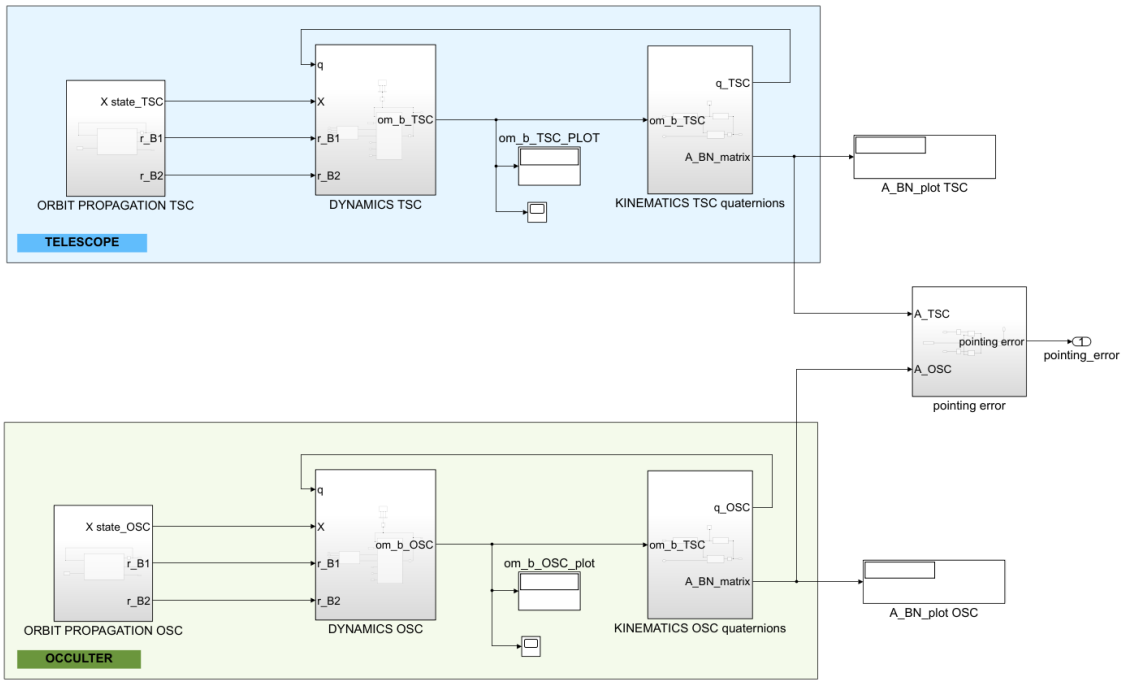

Figure 4.17: TSC - OSC Simulink block diagram

The attitude dynamics performance analysis presented in this section is conducted starting from the optimal orbits previously found. Sub-optimal control solutions will be therefore explored for different cases. First, a general overview of the Telescope - Occulter Formation free dynamics is reported to better understand the mission geometry with and

without SRP contribution. Then, an ideal attitude control optimization is proposed for both Lyapunov and Halo orbits. Figure 4.17 shows the block diagram built in *Simulink* environment, to replicate TSC (blue) and OSC (green) motion in a non-Keplerian Sun-Earth framework. The three rectangles, namely orbit propagation, dynamics and kinematics, inside the coloured boxes, have already been deeply analyzed in Chapter 2. The external block on the right instead, calculates the relative pointing angle between the two spacecrafts and it will be discussed in the next paragraphs. From now on, all the study will be carried out taking as reference the Telescope-Occulter Formation from *ECLIPSIS* mission [19], whose shape, dimensions and further details are reported in the Appendix A. The main mission goal is to observe exozodiacal dust resonant patterns via central star occultation. ECLIPSIS intends to leverage a cluster of small satellites flying in formation to demonstrate the feasibility of achieving the same mission objectives as a larger counterpart.

4.4.1. Free Attitude Dynamics

Free Attitude dynamics describes how spacecrafts motion would evolve naturally without control torque applied. Figures 4.18 and 4.19 demonstrates the effect of perturbations in an highly unstable environment such as Sun-Earth non-Keplerian framework, especially on small satellites. In particular, angular velocities profile and relative pointing angle are examined including and then removing the SRP term in the EoM 2.14.

Angular velocities

Both Lyapunov and Halo cases, reveal a similar behavior adding the SRP contribution. While the Telescope dynamics remains almost unchanged, the Occulter appears more influenced by the M_{SRP} disturbing torque. In fact, due to the presence of a large additional surface on OSC structure (1 diameter occulting disk), the resulting SRP force acting on it is significant with respect to TSC case.

Relative Pointing Angle

The same outcome can be also observed more clearly by looking at the TSC - OSC baseline relative pointing angle α_{err} plots in Figure 4.20. In order to perform good exoplanets observations, this parameter reported in Equation 4.5, should be ideally zero once control is applied, meaning that the two spacecrafts are perfectly aligned with their baseline. The graphs on the right, including SRP in the analysis, show a grater variation in values

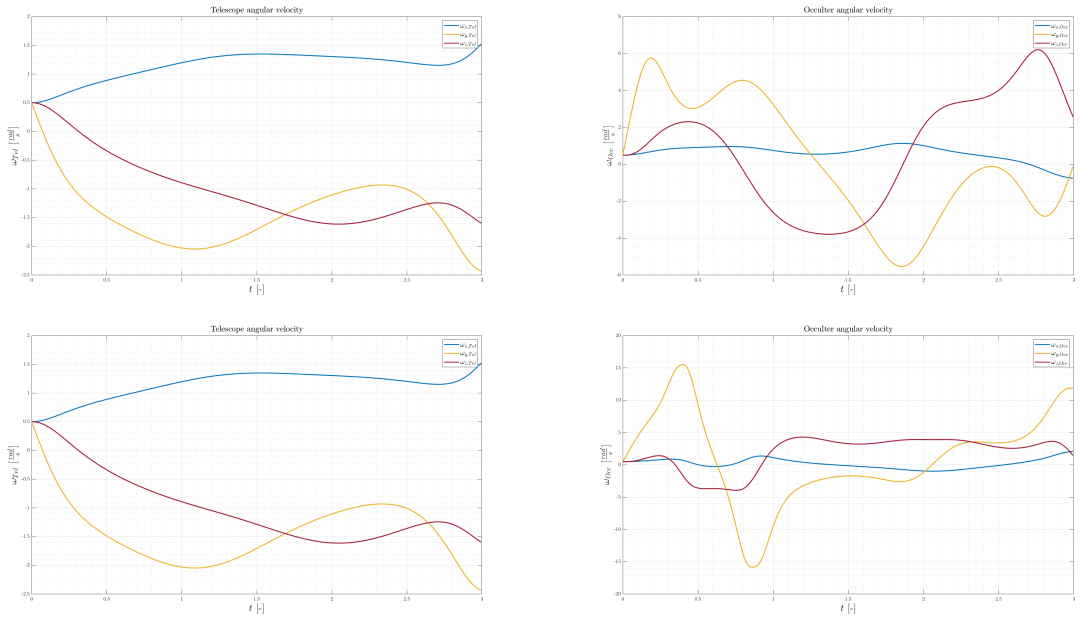

Figure 4.18: Telescope (left) - Occulter (right) angular velocities without (top) and with SRP (bottom) for Halo periodic - quasi periodic optimal configuration.

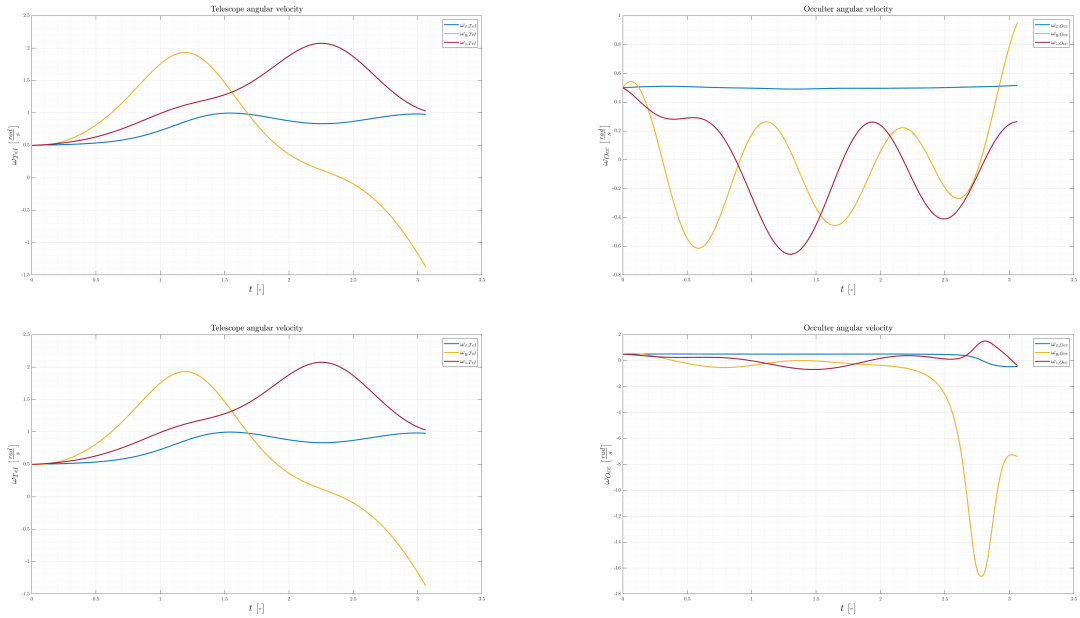

Figure 4.19: Telescope (left) - Occulter (right) angular velocities without (top) and with SRP (bottom) for planar Lyapunov periodic - quasi periodic optimal configuration.

during the overall orbital period.

$$\theta_{err,b} = \arccos(\hat{\mathbf{b}}_{\mathbf{N,TSC}} \cdot \ \hat{\mathbf{b}}_{\mathbf{N,OSC}}) \tag{4.5}$$

Here, $\hat{\mathbf{b}}_{\mathbf{N,TSC}}$ and $\hat{\mathbf{b}}_{\mathbf{N,OSC}}$ are the Telescope and Occulter pointing vectors expressed in the inertial frames. They have been calculated, according to Equation 4.6, starting from their counterparts $\hat{b}_{B,TSC}$ and $\hat{b}_{B,OSC}$ in the body reference systems equal to [1 0 0].

$$\hat{\mathbf{b}}_{\mathbf{N,i-th\ SC}} = \mathbf{A}_{\mathbf{BN,i-th\ SC}}\ \hat{\mathbf{b}}_{\mathbf{B,i-th\ SC}} \tag{4.6}$$

where $A_{BN,i-th\ SC}$ is the generic spacecraft rotation matrix from body to inertial frame describing its orientation.

The TSC body frame has in fact been defined such that the $x-axis$ points in the direction of the Telescope optical axis, the $y-axis$ and $z-axis$ point perpendicular to it and parallel to two of the four lateral Solar Panels (SP) surfaces. Similarly, the OSC body frame has $x-axis$ coincident with the Occulter normal direction (i.e. opposite to the Telescope pointing direction), and $y-axis$ and $z-axis$ as before.

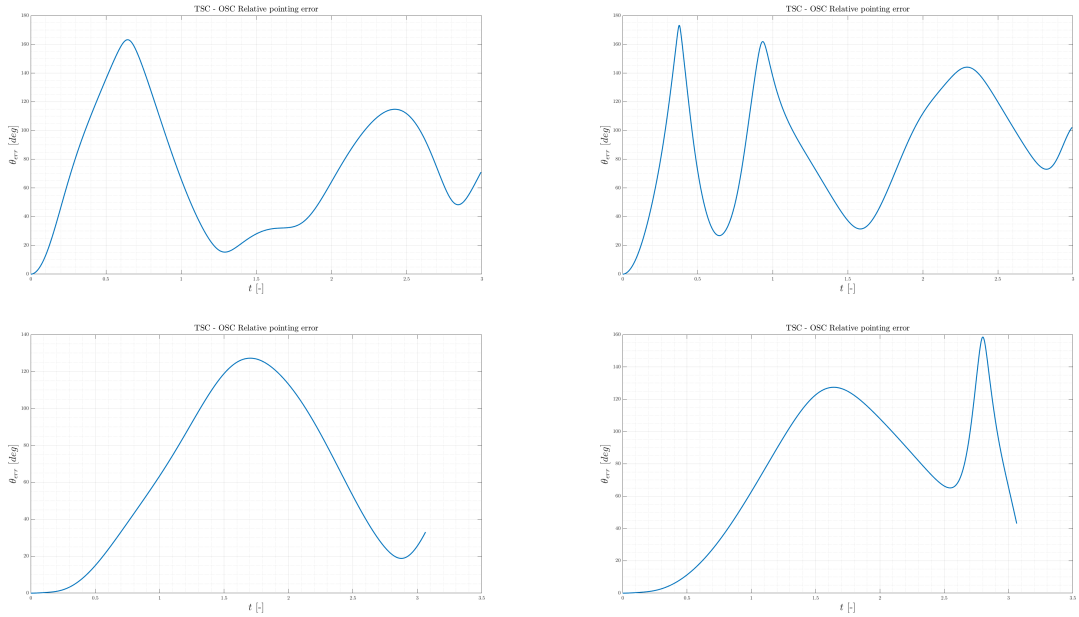

Figure 4.20: Telescope - Occulter relative poiting error without (left) and with SRP (right) for Halo (top) and planar Lyapunov (bottom) periodic - quasi periodic optimal configuration.

4.4.2. Controlled Attitude Dynamics

Attitude control is a crucial aspect for space missions that require precise pointing requirements, such as exoplanet observation using external coronagraph method. The success of these missions depends on achieving the very demanding pointing accuracy to capture clear images of the target exoplanet while blocking out the light from the host star. Attitude control is responsible for keeping the orientation of the spacecraft and instrument with respect to the target, aligning TSC and OSC with their baseline. In addition, the preceding sections have demonstrated the significance of the SRP effect on small spacecrafts. As a result, one of the main objectives of the attitude control system is to counteract external disturbances and maintain the pointing error within acceptable limits. Chapter 3 emphasized that for missions that utilize an external Occulter for exoplanet observation, there is a critical need for high-contrast imaging, thus necessitating stringent pointing accuracy requirements ($\leqslant 1\ mas$). The external Occulter should block out the light from the host star, which allows for the detection of fainter exoplanets that would otherwise be obscured by the star glare. However, this also means that any misalignment or pointing error between the Telescope and the Occulter can result in the starlight leaking through and interfering with the exoplanet observation.

The minimum value required for the pointing error in exoplanet observation missions using an external Occulter depends on several factors, including the size and distance of the target exoplanet, the brightness of the host star, and the sensitivity of the instrument. Generally, it must be within a fraction of the resolution of the instrument, which can be as small as a few milliarcseconds for clear exoplanets images. Achieving this level of pointing accuracy requires careful design and optimization of the attitude control system, including the use of fine pointing mechanisms and active control to compensate for disturbances and drift.

Hereinafter, a methodology for optimizing the ideal control torque $M_{control}$ to apply on both spacecrafts is presented. In order to verify mission pointing requirements, an approach similar to the one presented by Colombi [24] is followed.

Problem Definition

In order to find the best control able to maintain the correct FF pointing, the orbits have been divided in n different arcs. The choice of the number n strikes a balance between the accuracy of the state measure and computational cost. If n tends to infinity, the problem would become a continuous control rather than a discretized one, but this would also result in increased computational time. Therefore, a higher value of n allows for more

precise measurements and aids convergence, but also requires more computational effort. For this study the trajectories have been discretized using 1000 points.

For each arc the optimization problem has been defined by imposing the TSC and OSC control torques $M_{control,TSC}$ and $M_{control,OSC}$ as `fsolve` unknown optimization variables `x`. To create a square problem, the number of variables should be equal to the constraint objective function $F(x)$ dimension. For this reason, the objective function has the following expression.

$$\mathbf{F(x)} = \begin{cases} \hat{\mathbf{s}}_{\mathbf{B,TSC}} - \hat{\mathbf{x}}_{\mathbf{TSC}} \\ \hat{\mathbf{s}}_{\mathbf{B,OSC}} + \hat{\mathbf{x}}_{\mathbf{OSC}} \end{cases} \tag{4.7}$$

where $\hat{s}_{B,TSC}$ and $\hat{s}_{B,OSC}$, are the actual Telescope and Occulter target pointing vectors expressed in their body frames, calculated from the rotation matrix $\mathbf{R_{BN_{i-th\ SC}}}$ according to Equation 4.8.

$$\hat{\mathbf{s}}_{\mathbf{B,i-th\ SC}} = \mathbf{R_{BN_{i-th\ SC}}}\ \hat{\mathbf{s}}_{\mathbf{N,i-th\ SC}} \tag{4.8}$$

To cancel the star pointing errors, they should properly be aligned with their $x-axis$ vectors $\hat{x}_{TSC}$ and $\hat{x}_{OSC}$, built so that they coincides with Telescope and Occulter directions, as illustrated in Figure 4.21.

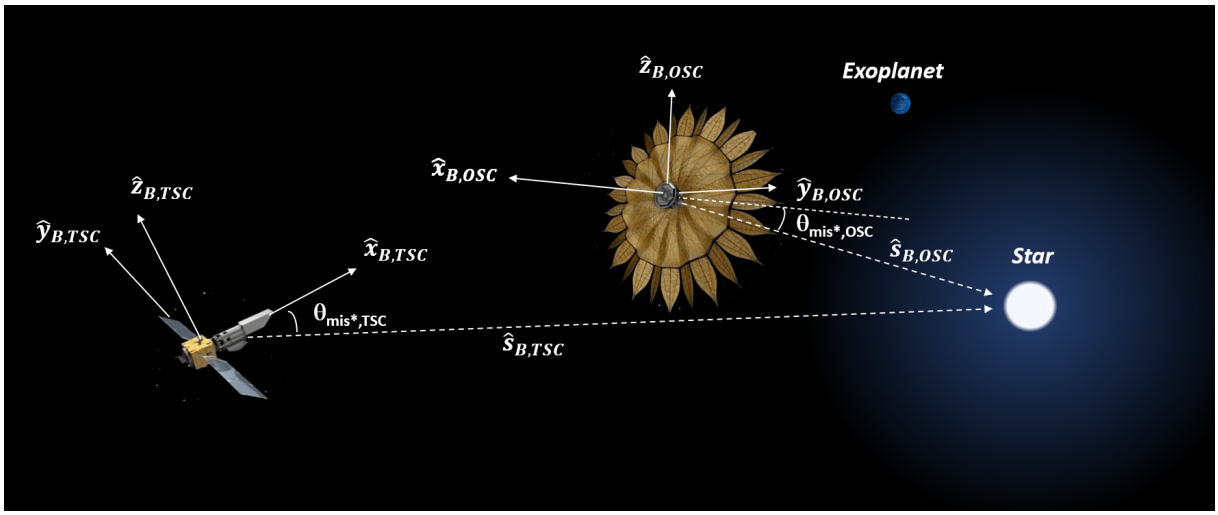

Figure 4.21: TSC-OSC body frames and formation geometry

For every segment of the trajectory, the optimal outcome from the previous arc is taken as the initial estimate for the successive control torque. The same approach is applied to the initial conditions of the propagator, i.e. $\mathbf{r_0}, \mathbf{v_0}, \mathbf{q_0}, \boldsymbol{\omega_0}$. However, as explained in the next section, to simulate the navigation state reconstruction measurements, an error in the state knowledge is introduced at each step.

State Reconstruction Simulation

Measurements are generated by adding random Gaussian noise to the expected state, as expressed in Equation 4.10. The noise vector is created using the `mvnrnd` function with zero mean and covariance matrix C_{noise}, which is computed from the standard deviation vectors σ and the identity matrix $\mathbf{I}$. The noise covariance matrix is given by:

$$\mathbf{C_{noise}} = \sigma^2 \, \mathbf{I} \tag{4.9}$$

Finally, the noisy measurements are obtained by adding the generated noise vector to the expected measurements:

$$\mathbf{x_{measure}} = \mathbf{x_{real}} + \mathbf{x_{noise}} \tag{4.10}$$

Sensors accuracy is sufficiently high, since the given standard deviations reported in Table 4.3 with respect to the mean values are quite small. Hence, true measurements only slightly differ from the expected ones. Bigger discrepancies between measured and real state could slow down problem convergence. Those σ values are retrieved from [34].

$\sigma_{\mathbf{r}}$	$\sigma_{\mathbf{v}}$	$\sigma_{\mathbf{q}}$	σ_{ω}
10 $[m]$	0.1 $[\frac{m}{s}]$	0.01 $[-]$	0.001 $[\frac{rad}{s}]$

Table 4.3: Optimal Performance summary

Ideal Control Torque

The presented set of Figures 4.22 displays the control torque required to maintain the desired pointing for two distinct orbital families, namely the Lyapunov and Halo orbits. Notably, the Lyapunov control torque is found to be approximately one order of magnitude lower than that required for Halo orbits. Additionally, the Lyapunov control torque exhibits a decreasing trend, indicating that it is easier to maintain the desired pointing for this orbital family. This may be attributed to the simpler structure of the Lyapunov orbits, which are planar in nature. This observation will be further supported by the pointing error plot in the next section. Furthermore, it is noted that the dynamics of the Halo orbits vary more rapidly than the Lyapunov orbits, resulting in a greater challenge in maintaining formation for this orbital family.

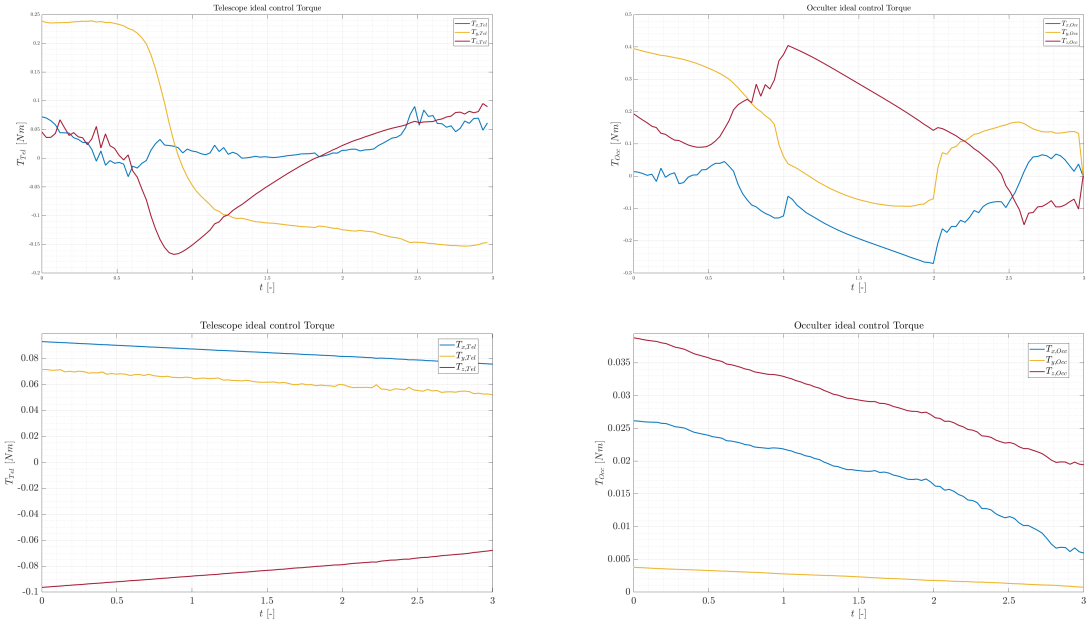

Figure 4.22: Telescope (left) - Occulter (right) control torque for Halo (top) and planar Lyapunov (bottom) periodic - quasi periodic optimal configuration.

Pointing Error

Figures 4.23 and 4.24 for the Halo and Lyapunov orbit cases show the baseline misalignment error for Telescope and Occulter, as well as the relative error between the two. The acceptable limits for the relative pointing error have already been presented in 4.2: 2.5 *mas* for Halo and 0.34 *mas* for Lyapunov.

As expected from the previous control torque plots, the Lyapunov orbit case illustrates lower pointing errors, remaining below the imposed limit for a good percentage of the simulation. This is likely due to the simpler planar structure of Lyapunov orbits, which makes them easier to control and maintain.

On the other hand, for the Halo periodic-quasi periodic orbit configurations there are few regions where the pointing requirements are not met. This is because Halo orbits are more unstable and exhibit faster dynamics compared to Lyapunov ones, making it more challenging to maintain the desired pointing accuracy.

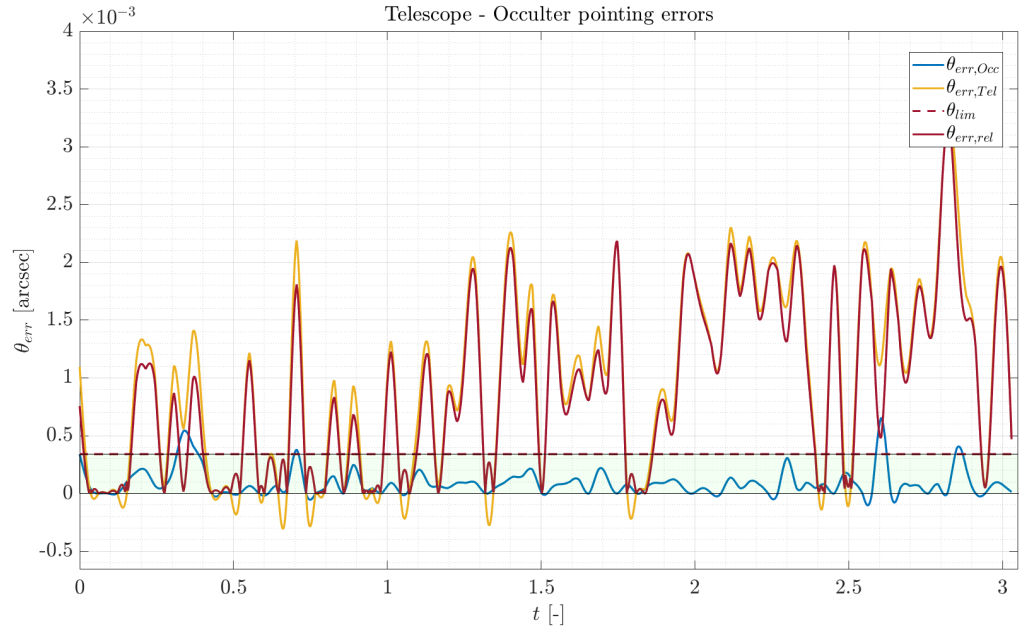

Figure 4.23: TSC - OSC misalignment errors for Lyapunov orbits

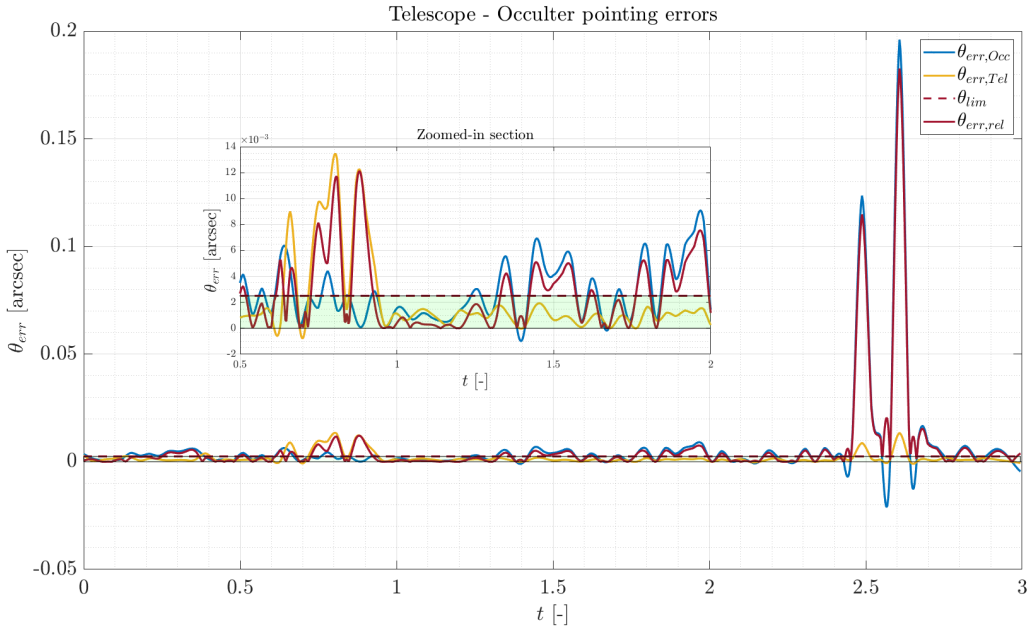

Figure 4.24: TSC - OSC baseline misalignment errors for Halo orbits

At this point, to verify the efficiency of the overall FF pointing control, the baseline $\theta_{err,baseline}$ and star misalignment errors $\theta_{err,star}$ are compared and then summed up. For both orbital families, Figures 4.25 and 4.26 show that $\theta_{err,star}$ results to be smaller than $\theta_{err,baseline}$. This is due to the fact that the attitude control problem has been conducted on accurately selected orbits, in which target visibility was already maximized. Total

misalignment error $\theta_{err,total}$ is depicted in red. For Lyapunov configurations, attitude requirements are met for the 24.7 % of the orbit, while 28.4 % for Halo. Halo QPOF still allows higher visibility conditions, consistently with previous attitude-free calculations. Moreover, incorporating attitude control to the analysis, those percentages slightly increased, as expected.

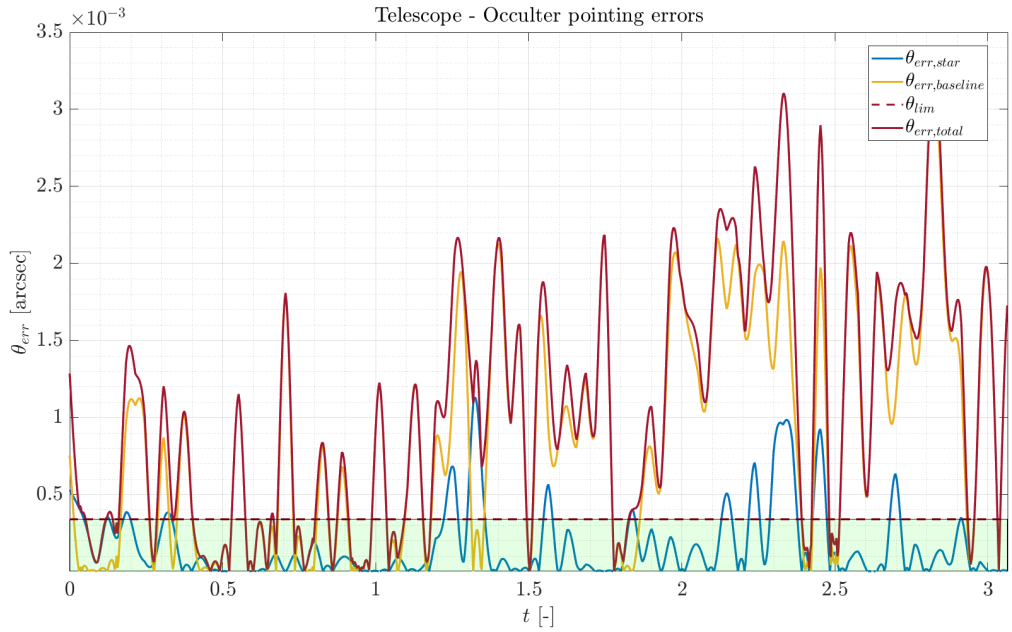

Figure 4.25: Baseline-Star misalignment errors for Lyapunov orbits

It should be pointed out that exoplanet observations are often done discontinuously, due to the reduced visibility of the target planet. In general, the necessary time to conduct a single scientific imaging can vary from 6 *hours* to 1 *day*. In ECLIPSIS mission [19] the duration of one observation lasts $\sim$ 9.6 *hours*, meaning that for an orbital period of 180 *days*, up to 430 *hours* are completely dedicated to the imaging of a selected target. It is important to note that in this work, the occultation method is demonstrated just for a to a single target, but the study could be greatly expanded if an on-board database is installed on the spacecrafts and a control algorithm is used to align the formation with the direction of the exoplanets present in the field of view at a given time as it has been proposed for [35] and [36] (respecting criteria in Table 3.1). This would significantly increase the scientific return of the mission. By improving the efficiency of observations, more data could be collected.

However, there are still various trajectories arc in which pointing minimum values are not met. Depending on the mission requirements and objectives, this may present a significant issue, as any degradation in pointing performance can directly impact the quality of the

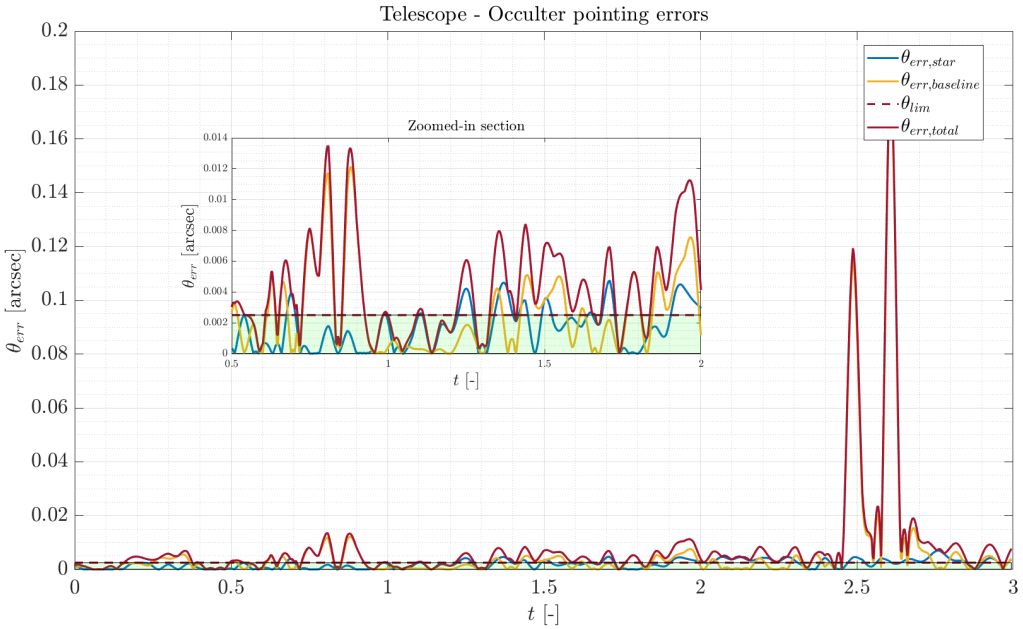

Figure 4.26: Baseline-Star misalignment errors for Halo orbits

observation. Therefore, either a reduction in performance should be analyzed, as it will be discussed in the upcoming section on performance degradation 4.4.2, or a better control strategy should be investigated to ensure that the pointing requirements can be met for the entire mission duration.

Performance Degradation

As anticipated in the previous section, the performances of an exoplanet observation mission exploting a Telescope-Occulter Formation can be significantly affected by the misalignment between the two instruments. In fact, the relative pointing error directly impacts the achievable signal-to-noise ratio SNR and contrast ratio CR of the observations.

Figure 4.27 reveals that when $\theta_{err,rel}$ grows, the SNR decreases because the amount of starlight that reaches the detector increases, making it more difficult to detect the faint light of the exoplanet. The green part of the graph represents the region in which CR assumes admissible values to perform good exoplanets imaging. The dotted line marks the limit of 10 under which the misalignment error is no more acceptable. Recalling Equation 3.7 it can be observed that the obtained pointing accuracy returns CR values in the green region. However, as it happens for the Halo case, when $\theta_{err,rel}$ reaches greater values, a degradation in the performance is expected.

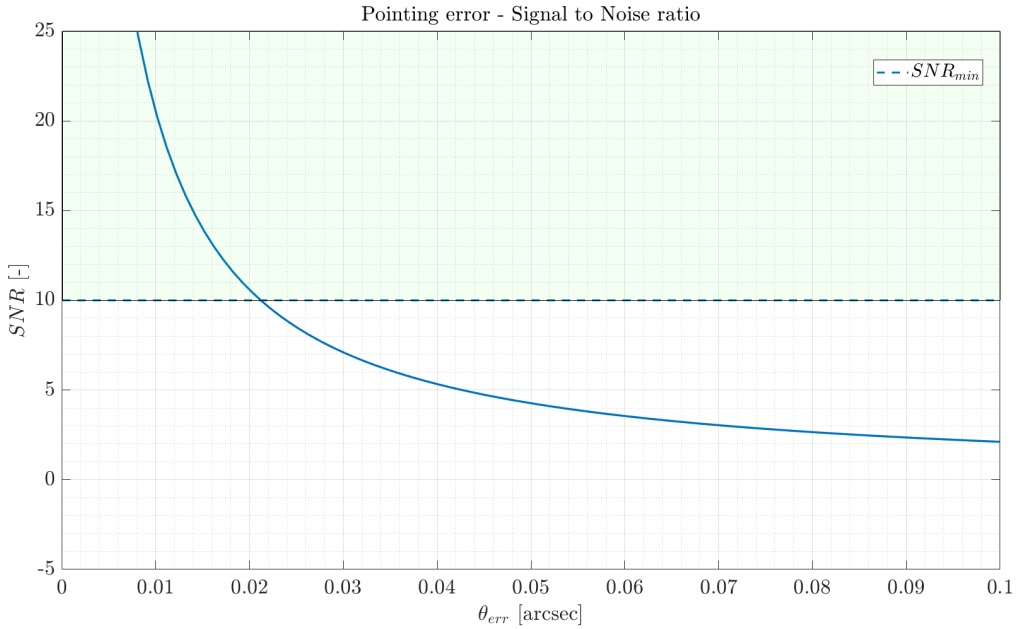

Figure 4.27: Pointing error - Signal to Noise Ratio

Similarly, the impact of pointing error on the contrast ratio can be explained using basic geometric optics. As the pointing error increases, the diffraction of starlight around the edge of the Occulter reduces the amount of starlight that is blocked, leading to a decrease in the contrast ratio as shown in Figure 4.28. Again, $\theta_{err,rel}$ obtained from the analysis allows the CR parameter to be inside the upper limit of 10^{-10}.

Angular Velocities

Finally, angular velocities plots provide valuable insights into the dynamics of each Formation configuration and the corresponding challenges in maintaining the desired pointing accuracy. From Figure 4.29 it can be noticed that, as anticipated, Halo orbit exhibits faster dynamics, leading to higher angular velocities compared to the Lyapunov case. This results in more frequent adjustments and corrections to the pointing, which can lead to increased pointing errors and potentially degrade the quality of the observation. However, for both cases, the angular velocities assumed by the Telescope and the Occulter are always relatively small.

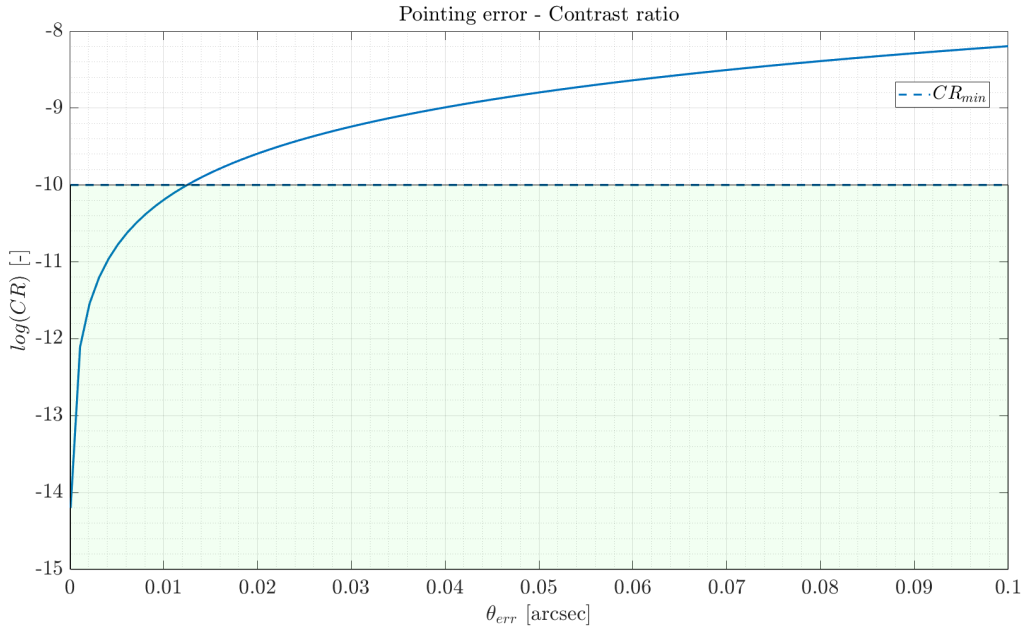

Figure 4.28: Pointing error - Contrast Ratio

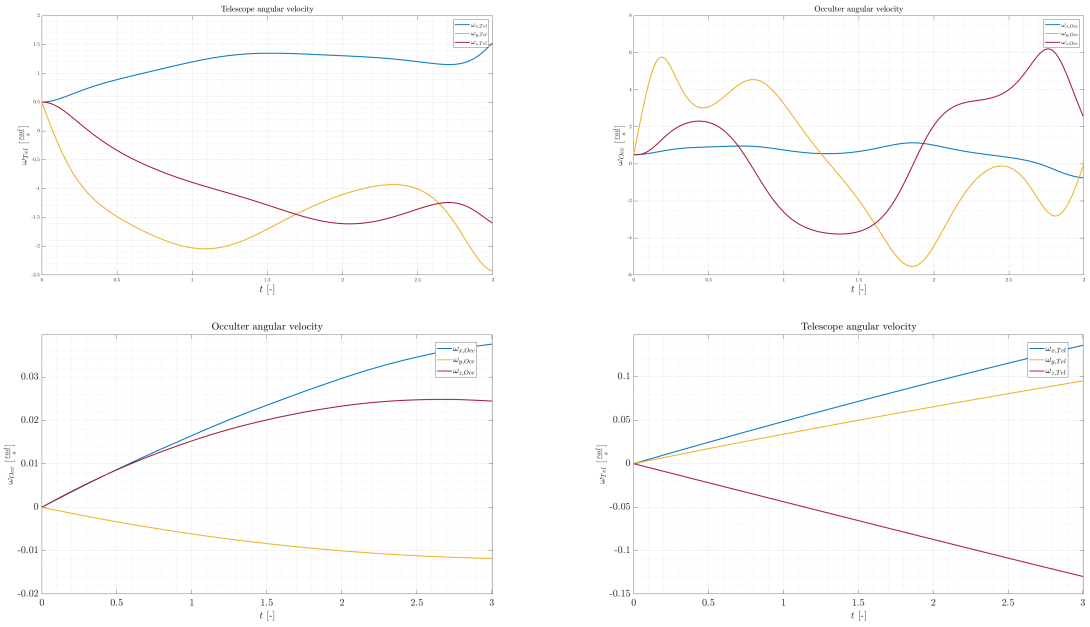

Figure 4.29: Telescope (left) - Occulter (right) angular velocities for Halo (top) and planar Lyapunov (bottom) periodic - quasi periodic optimal configuration.

4.5. Performance summary

The present study encompasses a performance analysis of a Telescope-Occulter FF mission, implemented for exoplanet observation by utilizing quasi-periodic orbits. Two dis-

tinct QPOFs, namely the Halo and the Lyapunov family, were compared in terms of respective sky coverage and time visibility. The results of the analysis revealed that both families allow exoplanet imaging for about one 1/4 of the overall period, requiring only a small OSC maneuver to repeat the same trajectory and continue the operations. Fixed the TSC-OSC geometrical parameters and observed that the baseline distance is in the order of $\sim 10^4 - 10^5\ km$, the constraints on the maximum misalignment error are derived.

At this point, a study on the sub-optimal solutions is performed adding attitude ideal control to the problem to verify if such demanding pointing accuracies ($\theta_{err,baseline}$ and $\theta_{err,star}$) can be reached with a feasible control moment applied on the spacecrafts. Calculation shows that time in visibility of the target slightly increments for both optimal orbits configurations. To increase scientific return, different solutions are viable. Performance degradation with pointing error can be taken into account to understand up to which point good observations can be done. Another option to enhance mission performances could be reducing baseline during scientific imaging or designing a bigger Star-shade radius. In any case the spacecrafts shall be equipped with very high-performing Attitude Determination and Control System (ADCS) to guarantee *arcsecond* pointing accuracy.

Tables 4.4 and 4.5 summarize the results of the optimal and sub-optimal performance analysis.

	T_{orb}	b	A_{perc}	T_{vis}	Δv
Lyapunov	178.15 $[days]$	$\sim 10^5$ $[km]$	14.3%	22.9%	$0.507\frac{m}{s}$
Halo	174.16 $[days]$	$\sim 10^4$ $[km]$	16.5%	25.4%	$0.610\frac{m}{s}$

Table 4.4: Optimal Performance summary

	$M_{control}$	θ_{err}	T_{vis}	SNR	CR
Lyapunov	10^{-2} $[Nm]$	~ 0.1 $[arcsec]$	24.7 %	> 10	$< 10^{-10}$
Halo	10^{-1} $[Nm]$	~ 1 $[arcsec]$	28.4 %	< 10	$> 10^{-10}$

Table 4.5: Sub - Optimal Performance summary

4.6. Proposed ADCS Architecture

The technological objectives of the mission pertain to fulfilling the rigorous scientific requirements of pointing accuracy, stability, and maneuverability. The need to observe for prolonged time and with great precision diverse astronomical objects necessitates an attitude control subsystem that can achieve arcsecond pointing accuracy and maintain the correct orientation with minimal oscillations over a prolonged duration.

The ADCS subsystem design is based on these mission constraints. To meet the requirement of a $3-axis$ stabilized platform with high accuracy, the ADCS architecture should rely on primary attitude sensors and actuators such as very performing star trackers and reaction wheels, respectively to determine and control precisely TSC and OSC state. The proposed architecture follows together with the description of each sensor and actuators that should be mounted on both spacecrafts.

- **IMU**: The Inertial Measurement Unit (IMU) provides angular velocities and accelerations information.
- **Sun Sensors**: Set of 4 sun sensors in order to provide full sky coverage.
- **Earth Sensor**: Sensor based on optical detector for earth bearing determination. Useful for attitude determination as well as for state (position, velocity) determination.
- **Star Trackers**: 2 fine star sensors for precise attitude determination with an accuracy under 1 arcsec and a Field of View (FOV) of 10°. Both shall point to the deep space and one of them shall also point in the same direction of the telescope axis.
- **WAC**: The Wide Angle Camera (WAC) provides the proximity FF capability, in fact, it is employed to perform a course search of the observable targets. The WAC shall have a 10° FOV.
- **LOS**: The Low Order Sensor (LOS) is the feedback coming from the telescope. For this reason, it is not part of the AOCS budgets since it comes with the payload and it is used as a Narrow Angle Camer NAC.
- **RW**: A set of Reaction Wheels (RWs) is used to apply a torque on the Telescope and Occulter. They are in number of 4 in order to have redundancy for risk mitigation. The total angular momentum of each RW shall be higher than 0.1 Nms in order to fully control the S/C also in the worst-case scenario. While the maximum torque should be greater than 0.5 Nm in order to be consistent with results in Figure 4.22. The reaction wheels would control and stabilize the attitude along the prescribed

pointing direction, exploiting the pointing error angle as a guidance parameter.

5 | Conclusions

5.1. Summary

This work covered various aspects for the design and optimization of a successful exoplanets observation mission by means of a Telescope-Occulter Formation on QPOFs configurations. The background knowledge of non-Keplerian dynamical models has been presented, including the formulations used for modeling the Solar Radiation Pressure effect on Euler Equations, as well as the generation of Periodic and Quasi-Periodic Halo and Lyapunov orbits.

The mission design requirements have been then extensively discussed, such as the Telescope-Occulter baseline, star-observer distance, and star-exoplanet distance. A certain numbers of possible targets have been identified as potential exoplanets observable with the Starshade method. The design of the Occulter spacecraft has been presented from both a geometric and engineering perspective, including the creation of the Occulter shape and the optimal number of petals required to obtain a good diffraction pattern.

Then, a performance analysis of different Telescope-Occulter orbital configurations has been conducted. Performance metrics, such as selected target area, visibility time, and sky coverage, have been defined, and a comparison between Halo and Lyapunov possible orbital couples has been discussed. The solutions with the most promising performances have been therefore analyzed, and attitude dynamics has been added to the problem. Ideal control torque with Solar Radiation Pressure contribution to the equations of motion has been computed to give a quantitative estimation of the control effort required by the overall system. The stability of the attitude has been examined through the analysis of the angular velocities of the Telescope and the Occulter, and the relative pointing angle between the spacecrafts has been evaluated to validate the analysis.

In the next sections, final remarks will encompass a critical discussion of the contributions and limitations of this work, and provide insights for potential future advancements in this area of research.

5.2. Contributions

This work made several contributions towards the design and the optimization of external Occulter missions for exoplanets observation. An innovative strategy combining the novelties related to the application of an external coronograph method, together with the choice of two small satellites flying information on cost-effective and higher-performing Quasi-Periodic orbital families has been proposed and discussed. As well, extensive analysis has focused on the achievable Line of Sight accuracy, crucial aspect for the FF maintenance. The research objectives presented in Section 1.2.1 are therefore hereafter re-examined:

OBJ 1. Performances of Telescope-Occulter Formation for exoplanets direct observation in non-Keplerian Sun-Earth environment has been investigated. Halo and Planar Lyapunov QPOFs have been compared in terms of sky coverage and visibility time. The results of the analysis revealed that both families allow exoplanet imaging for about 1/4 of the overall period. Nevertheless, recalling the shape of the two orbital families, it can be clearly noticed that being the Lyapunov orbits planar, their baseline could ideally cover less region to be observed in the sky. On the contrary, being more inclined trajectories, the elevation vector of the Line of Sight from TSC to OSC for the Halo orbits, spans a broader observation area. Consequently, one would expect performances in terms of Sky Coverage for the Halo case to be higher than Lyapunov ones. Analysis validated the predicted results. In fact, maximum performances are obtained for Halo orbital combinations. However, due to the introduction of a phase shift, a wider area of sky observation is achievable also with the Lyapunov family. This justifies the relatively small difference in the A_{cov} peaks for Halo 16.5% compared to 14.3% for the Lyapunov. It is worth mentioning that in this work, the occultation method has been demonstrated for a single target just as example, but the study could be greatly expanded if an on-board database was installed on the spacecrafts and a control algorithm was used to align the formation with the direction of the exoplanets present in the FoV at any given time. This would significantly increase the scientific return of the mission. By improving the efficiency of observations (i.e. sky coverage and visibility time), more data could be collected.

OBJ 2. Different quasi-periodic orbital configurations in CR3BP (Circular Restricted 3-Body Problem) framework to optimize exoplanets observation has been proposed. In fact, large numbers of periodic and quasi-periodic combinations (univocally defined by the frequencies Ω_0 and Ω_1), where to place respectively the TSC and OSC, has been studied. Moreover, thanks to the introduction of the additional phase shift parameter θ_{shift}, the total observation region visible with a specific configuration increased. The

work has demonstrated the feasibility of exploiting Periodic and Quasi-Periodic orbits in the Sun-Earth non-Keplerian framework for exoplanet imaging purposes. It has been noticed that, as expected, using QPOFs significantly reduced mission propulsion budget. In fact, without considering the small velocity adjustment to close the OSC quasi-periodic trajectory (in the order of $\sim 1\ \frac{m}{s}$), the natural dynamics evolution of the spacecrafts in such environment guarantees a stable Formation baseline. Correction on the OSC could be even avoided transitioning from different consecutive toroids. In this case the Formation would continue naturally without requiring additional propellant to return to the previous trajectory. This is achieved by means of a continuation schemes, which allow the spacecrafts to smoothly move from one orbit to another, improving mission efficiency and flexibility.

OBJ 3. Sub-optimal TSC and OSC attitude control solutions to reach required LoS pointing accuracy are found. In fact, once obtained the optimal orbital configurations (reported in Table 4.4) and the corresponding baseline distances b for each QPOFs, the rotational dynamics has been introduced to the problem and attitude requirements have been assessed in terms of minimum IWA and total pointing error θ_{err}. In particular, pointing requirements for Lyapunov orbits appeared to be more demanding than Halo ones (respectively < 0.34 $[mas]$ and < 2.5 $[mas]$), since they deal with higher baseline ranges. However, the Lyapunov control torque is found to be approximately one order of magnitude lower than that required for Halo orbits. Halo orbit exhibits faster dynamics, leading to higher angular velocities compared to the Lyapunov case. Then, to verify the efficiency of the overall FF pointing control, the baseline $\theta_{err,baseline}$ and star misalignment errors $\theta_{err,star}$ have been compared and summed up. For both orbital families, $\theta_{err,star}$ resulted to be smaller than $\theta_{err,baseline}$. This is due to the fact that the attitude control problem has been conducted on accurately selected orbits, in which target visibility was already maximized. Analysis showed that for Lyapunov configurations, attitude requirements are met for the 24.7 % of the orbit, while 28.4 % for Halo. Halo QPOF still allows higher visibility conditions, consistently with previous attitude-free calculations. Incorporating attitude control to the analysis, those percentages slightly increased, as expected. However, there are still various trajectories arc in which pointing minimum values are not met. Depending on the mission requirements and objectives, this may present a significant issue, as any degradation in pointing performance can directly impact the quality of the observation. Therefore, either a reduction in performance should be considered, or a better control strategy should be investigated to ensure that the pointing requirements can be met for the entire mission duration. In this work the impact of $\theta_{err,total}$

on the Contrast Ratio CR and Signal to Noise Ratio (SNR) has been examined using basic geometric optics. Performance degradation analysis revealed that when θ_{err} grows, the SNR decreases because the amount of starlight that reaches the detector increases, making it more difficult to detect the faint light of the exoplanet, but there are still admissible $\theta_{err,total}$ ranges in which SNR is still greater than the imposed limit > 10 to perform good exoplanets imaging. Similar consideration has been presented for the CR parameter.

OBJ 4. Finally, one the primary objectives of this thesis was to develop a general methodology and set of performance guidelines that could be adapted to a wide variety of scenarios (i.e. instrumentation characteristics, mission analysis constraints, type and number of desired observations) in future Star-shade projects. By providing a flexible framework that can be tailored to different scientific requirements, like the one proposed in this work, this approach aims to facilitate the planning and execution of future direct imaging missions.

In conclusion, this work has provided a comprehensive study of various aspects for exoplanet direct imaging observation whose contribution could potentially enable future missions to achieve high-quality observations with reduced costs. Further research is required to explore their full potential and limitations.

5.3. Limitations

While the proposed approach for observing exoplanets holds immense potential for advancing our understanding of the universe and facilitating new discoveries, it is imperative to recognize its inherent limitations. These limitations may arise from various factors, such as design complexities, technological constraints, or fundamental physical limitations. Identifying and addressing these bottlenecks is crucial to ensure that the proposed work can deliver accurate and meaningful results. In this section are examined the weak points associated with the proposed approach, highlighting how they may affect its effectiveness and reliability.

For example, while a high number of design variables may offer more flexibility to delineate instrument properties for observing exoplanets, it may be challenging to create realistic test scenarios that can adequately assess its performance across all the design parameters.

Another impeding factor could be represented by the Formation communication bandwidth. Due to the large distances involved in exoplanet observation missions, it could be hard to establish reliable communication links between the spacecrafts. This can limit the

amount of data that can be transmitted back to Earth and the relative navigation efficiency, if required. Data compression techniques or advanced signal processing algorithms could be needed.

This aspect leads to an additional interesting point to be discussed, namely the synchronization alignment of the spacecrafts. It is necessary for maintaining the proper separation distance between the TSC and OSC. If the synchronization is not precise, it can result in significant errors in the observations, as the Occulter may not block the starlight from the exoplanet accurately. Several factors can impact the precision of synchronization, such as the accuracy of the spacecraft positioning and the quality of the communication links itself between the spacecrafts. To achieve precised synchronization, the mission may require advanced techniques such as laser ranging or time transfer, which can provide accurate measurements of the distance and time between the spacecrafts.

For what concerns physical limitations of the system, the problem of deploying and operating a petal-shaped Occulter for exoplanet observation should be considered. In particular, introduction of advanced materials, complex deployment mechanisms for such a large surface could represent a critical issue to overcome. Including a deep structural analysis on Occulter dynamical model may be necessary in future works.

5.4. Future Work

To further enhance the results and potential of this thesis, future works can focus on addressing the limitations and technical challenges associated with an exoplanet observation mission using Telescope-Occulter Formation.

One promising direction for future work is incorporating attitude analysis alongside orbital analysis from the beginning of the problem. This could be done in order to obtain different and eventually more optimal solutions, even if this would increase the complexity and computational time required. Moreover, doing so would mean developing more sophisticated models to account for attitude dynamics and control, as well as optimizing the interplay between attitude and orbital motion using a 6DoF dynamics.

Another promising point is the investigation of the feasibility and performance of QPOFs using multiple Occulters in Formation with the Telescope. Multiple OSC could be placed on the same toroid but at different initial points in order to obtain an almost full coverage of the sky and increase the frequency of observations. Additionally, future work could focus on better understanding and managing the passage of exoplanets through the field of view, including developing algorithms to automatically identify and track the exoplanet

and its star system, applying the minimal control torque to optimizing the scanning.

Furthermore, although a Circular Restricted Three Body model provides a simplified representation of the system, it is sufficient for the preliminary analysis and feasibility study of the exoplanet observation mission. However, high-fidelity dynamical models could return more detailed information regarding the behavior of the system and they could potentially lead to better performances. By incorporating more accurate dynamical models and control strategies, the Formation could better handle the uncertainties and disturbances to which the spacecrafts are subjected (such as SRP), bringing the mission to a higher level of reliability, especially when high demanding pointing accuracy is needed for the mission realization . Moreover, as anticipated in the previous section, including structural analysis of the Occulters in the dynamical model, as it has been done in [25], would provide a more comprehensive and accurate representation of the system, which could be beneficial for the overall success of the mission.

In conclusion, by pursuing these avenues of future work, we can expand the potential of this research and lead to significant advancements in the field of exoplanet observation.

5.5. Final Remarks

In summary, this research has demonstrated the potential of a Telescope-Occulter Formation Flying mission for exoplanet observation using Quasi-Periodic Orbital Families. The utilization of an External Coronograph method with a Telescope enables the blocking of light from the star, resulting in the reduction of the contrast ratio between the exoplanet and its host star, thereby permitting the detection of fainter planets. The use of Quasi-Periodic Orbits provides several benefits, including increased stability and reduced fuel consumption for the spacecrafts with respect to other orbits. A trade-off in the orbital family selection should be conducted based on the starting mission requirements. Both Halo and Lyapunov solutions present good possible configurations to perform exoplanets observation reaching the needed pointing accuracy, applying a feasible control torque. Although this approach has presented certain limitations, these can be overcome through the suggested future developments. Furthermore, the study offers valuable insights into the utilization of Telescope-Occulter Formation Flying missions for exoplanet observation, that could hopefully encourage further research in this area.

Bibliography

[1] Lyman Spitzer. The beginnings and future of space astronomy. *American Scientist*, 50(3):473–484, 1962.

[2] Natalie M Batalha. Exploring exoplanet populations with nasa's kepler mission. *Proceedings of the National Academy of Sciences*, 111(35):12647–12654, 2014.

[3] Brice-Olivier Demory, David Ehrenreich, Didier Queloz, Sara Seager, Ronald Gilliland, William J Chaplin, Charles Proffitt, Michael Gillon, Maximilian N Günther, Björn Benneke, et al. Hubble space telescope search for the transit of the earth-mass exoplanet α centauri b b. *Monthly Notices of the Royal Astronomical Society*, 450(2):2043–2051, 2015.

[4] Natalia M Guerrero, S Seager, Chelsea X Huang, Andrew Vanderburg, Aylin Garcia Soto, Ismael Mireles, Katharine Hesse, William Fong, Ana Glidden, Avi Shporer, et al. The tess objects of interest catalog from the tess prime mission. *The Astrophysical Journal Supplement Series*, 254(2):39, 2021.

[5] Charles Beichman, Bjoern Benneke, Heather Knutson, Roger Smith, Pierre-Olivier Lagage, Courtney Dressing, David Latham, Jonathan Lunine, Stephan Birkmann, Pierre Ferruit, et al. Observations of transiting exoplanets with the james webb space telescope (jwst). *Publications of the Astronomical Society of the Pacific*, 126(946):1134, 2014.

[6] Óscar Carrión-González, A García Muñoz, NC Santos, J Cabrera, Sz Csizmadia, and Heike Rauer. Catalogue of exoplanets accessible in reflected starlight to the nancy grace roman space telescope-population study and prospects for phase-curve measurements. *Astronomy & Astrophysics*, 651:A7, 2021.

[7] Engineering National Academies of Sciences and Committee on Exoplanet Science Strategy Medicine. Exoplanet science strategy. *The National Academies Press*, 2018.

[8] Matthew R Bolcar, Steve Aloezos, Vincent T Bly, Christine Collins, Julie Crooke, Courtney D Dressing, Lou Fantano, Lee D Feinberg, Kevin France, Gene Gochar, et al. The large uv/optical/infrared surveyor (luvoir): decadal mission concept design

update. In *UV/Optical/IR Space Telescopes and Instruments: Innovative Technologies and Concepts VIII*, volume 10398, pages 79–102. SPIE, 2017.

[9] B Scott Gaudi, Sara Seager, Bertrand Mennesson, Alina Kiessling, Keith Warfield, Kerri Cahoy, John T Clarke, Shawn Domagal-Goldman, Lee Feinberg, Olivier Guyon, et al. The habitable exoplanet observatory (habex) mission concept study final report. *arXiv preprint arXiv:2001.06683*, 2020.

[10] David Leisawitz, Edward Amatucci, Lynn Allen, Jonathan Arenberg, Lee Armus, Cara Battersby, James Bauer, Bobby G Beaman, Ray Bell, Porfirio Beltran, et al. Origins space telescope: baseline mission concept. *Journal of Astronomical Telescopes, Instruments, and Systems*, 7(1):011002–011002, 2021.

[11] Ziqi Dai, Dong Ni, Lizhuang Pan, and Yiheng Zhu. Five methods of exoplanet detection. In *Journal of Physics: Conference Series*, volume 2012, page 012135. IOP Publishing, 2021.

[12] Andrea Fortier, Thomas Beck, Willy Benz, Christopher Broeg, Virginie Cessa, David Ehrenreich, and Nicolas Thomas. Cheops: a space telescope for ultra-high precision photometry of exoplanet transits. In *Space Telescopes and Instrumentation 2014: Optical, Infrared, and Millimeter Wave*, volume 9143, pages 750–761. SPIE, 2014.

[13] Michel Mayor and Didier Queloz. A jupiter-mass companion to a solar-type star. *nature*, 378(6555):355–359, 1995.

[14] David J Des Marais, Martin O Harwit, Kenneth W Jucks, James F Kasting, Douglas NC Lin, Jonathan I Lunine, Jean Schneider, Sara Seager, Wesley A Traub, and Neville J Woolf. Remote sensing of planetary properties and biosignatures on extrasolar terrestrial planets. *Astrobiology*, 2(2):153–181, 2002.

[15] Olivier Guyon. High performance pupil remapping using a single-mode fiber for high contrast imaging. *Publications of the Astronomical Society of the Pacific*, 115(810):748–754, 2003.

[16] Robert J. Vanderbei, David N. Spergel, and N. Jeremy Kasdin. The challenge of direct imaging of exo-earths: Unveiling the impact of occulter shape on planet detection. *The Astrophysical Journal*, 647(1):L59–L62, 2006.

[17] Marc J. Kuchner and Wesley A. Traub. A coronagraph with a band-limited mask for finding terrestrial planets. *The Astrophysical Journal*, 570(2):900–908, 2002.

[18] N. Jeremy Kasdin and Robert J. Vanderbei. High-contrast imaging of exoplanets with

a phase-induced amplitude apodization coronagraph. *The Astrophysical Journal*, 582(2):1147–1161, 2003.

[19] Cravedi S. et al. Chillemi E., Colombi F. Exozodiacal dust imaging for near stars. Technical report, Politecnico di Milano, 7 2017.

[20] Daniele Barberi Spirito. Martian assets navigation service through mars-phobos multi-body regime exploitation for constellation design. Master's thesis, Politecnico di Milano, 2020.

[21] David L Richardson. Analytic construction of periodic orbits about the collinear points. *Celestial mechanics*, 22(3):241–253, 1980.

[22] Andrea Capannolo. Dynamics, guidance and control of reconfigurable spacecraft formations in multibody environments. 2022.

[23] June Barrow-Green. *Poincaré and the three body problem*. Number 11. American Mathematical Soc., 1997.

[24] Francesco Colombi, Andrea Colagrossi, and Michèle Lavagna. Characterisation of 6dof natural and controlled relative dynamics in cislunar space. *Acta Astronautica*, 196:369–379, 2022.

[25] Andrea Colagrossi. *Absolute and Relative 6DOF Dynamics, Guidance and Control for Large Space Structures in Cislunar Environment*. PhD thesis, Politecnico di Milano, 2018.

[26] John W Evans. A photometer for measurement of sky brightness near the sun. *JOSA*, 38(12):1083–1085, 1948.

[27] Sébastien Vivès, Philippe Lamy, Michel Saisse, JL Boit, and Patrick Levacher. The giant externally occulted coronagraph aspiics for the proba-3 formation flying mission. In *Solar Physics and Space Weather Instrumentation II*, volume 6689, pages 105–116. SPIE, 2007.

[28] Robert J Vanderbei, Eric Cady, and N Jeremy Kasdin. Optimal occulter design for finding extrasolar planets. *The Astrophysical Journal*, 665(1):794, 2007.

[29] Webster Cash. Detection of earth-like planets around nearby stars using a petal-shaped occulter. *Nature*, 442(7098):51–53, 2006.

[30] Adam W Koenig, Simone D'Amico, Bruce Macintosh, and Charles J Titus. A pareto-optimal characterization of miniaturized distributed occulter/telescope systems. In

Techniques and Instrumentation for Detection of Exoplanets VII, volume 9605, pages 355–374. SPIE, 2015.

[31] A.J. Lovell and D.W. Wilson. Design of occulters for terrestrial planet finder coronagraphs using shaped pupil masks. *Journal of the Optical Society of America*, 2004.

[32] N Jeremy Kasdin, Robert Joseph Vanderbei, Dan Sirbu, J Samuels, S Shaklan, D Lisman, M Thomson, E Cady, and S Martin. Recent progress on external occulter technology for imaging exosolar planets. In *2013 IEEE Aerospace Conference*, pages 1–14. IEEE, 2013.

[33] NASA Exoplanet Archive. A Service of NASA Exoplanet Science Institute. `https://exoplanetarchive.ipac.caltech.edu/`, Accessed 2023-03-26.

[34] Anthony Harness, Ann Shipley, and Steve Warwick. Development of formation flying sensors for external occulters. 2015.

[35] Egemen Kolemen and N Jeremy Kasdin. Optimization of an occulter-based extrasolar-planet-imaging mission. *Journal of guidance, control, and dynamics*, 35(1):172–185, 2012.

[36] Eric Cady, Ruslan Belikov, Philip Dumont, Robert Egerman, N Jeremy Kasdin, Roger Linfield, Doug Lisman, Dmitry Savransky, Sara Seager, Stuart Shaklan, et al. Design of a telescope-occulter system for theia. *arXiv preprint arXiv:0912.2938*, 2009.

[37] Lavagna M. Capannolo A., Pasquale A. High-order polynomial continuation method for trajectory design in non-keplerian environments. *Celestial Mechanics and Dynamical Astronomy*, 2021.

[38] Lavagna M. Capannolo A., Ferrari F. Families of bounded orbits near binary asteroid 65803 didymos. *JOURNAL OF GUIDANCE, CONTROL, AND DYNAMICS*, pages 189–198, 2019.

[39] Fiore F. Trenti M. Tagliaferri G., Lavagna M. Cubesat with high performance for skyhopper.

[40] Andrea Colagrossi. Coupled dynamics around irregularly-shaped bodies with enhanced gravity field modelling. Master's thesis, Politecnico di Milano, 2014.

[41] Stefano Silvestrini. *AI-augmented Guidance, Navigation and Control for Proximity Operations of Distributed Systems*. PhD thesis, Politecnico di Milano, 2020.

[42] Simone D'Amico. *Autonomous formation flying in low earth orbit*. PhD thesis, TU Delft, 2010.

[43] Danwei Wang, Baolin Wu, and Eng Kee Poh Chung. Satellite formation flying. *Springer Singapore) URL https://doi. org/10*, 1007:978–981, 2017.

[44] Robert A Werner. Spherical harmonic coefficients for the potential of a constant-density polyhedron. *Computers & Geosciences*, 23(10), 1997.

[45] Andrea Pasquale. Small bodies gravity field on-board learning and navigation. 2019.

[46] Wang Sang Koon, Martin W Lo, Jerrold E Marsden, and Shane D Ross. Dynamical systems, the three-body problem and space mission design. World Scientific, 2000.

[47] RenŽe Dotson et al. *Exoplanets*. University of Arizona Press, 2010.

[48] Jesse Leitner. Formation flying system design for a planet-finding telescope-occulter system. In *UV/Optical/IR Space Telescopes: Innovative Technologies and Concepts III*, volume 6687, pages 477–486. SPIE, 2007.

[49] W Cash, E Schindhelm, J Arenberg, A Lo, R Polidan, J Kasdin, R Vanderbei, S Kilston, and C Noecker. External occulters for direct observation of exoplanets: an overview. *UV/Optical/IR Space Telescopes: Innovative Technologies and Concepts III*, 6687:381–394, 2007.

[50] Davide Guzzetti and Kathleen C Howell. Coupled orbit-attitude dynamics in the three-body problem: A family of orbit-attitude periodic solutions. In *AIAA/AAS Astrodynamics Specialist Conference*, page 4100, 2014.

[51] Zubin P Olikara and Daniel J Scheeres. Numerical method for computing quasi-periodic orbits and their stability in the restricted three-body problem. *Advances in the Astronautical Sciences*, 145(911-930):911–930, 2012.

[52] L Tarabini Castellani, JS Llorente, F Sjoberg, B Jacobsson, F Teston, F Burger, and A Cropp. Proba-3 formation flying guidance navigation and control.

[53] J Salvador Llorente, Alfredo Agenjo, Carmelo Carrascosa, Cristina de Negueruela, Agnes Mestreau-Garreau, Alexander Cropp, and Andrea Santovincenzo. Proba-3: Precise formation flying demonstration mission. *Acta Astronautica*, 82(1):38–46, 2013.

[54] Daniel P Scharf, Stefan R Martin, Carl Christian Liebe, Zahidul H Rahman, Carl R Seubert, Martin Charles Noecker, and George H Purcell. Precision formation flying at megameter separations for exoplanet characterization. *Acta Astronautica*, 123:420–434, 2016.

[55] Ariadna Farres, Cassandra Webster, and David Folta. High fidelity modeling of srp

and its effect on the relative motion of starshade and wfirst. In *2018 Space Flight Mechanics Meeting*, page 2227, 2018.

A | Appendix

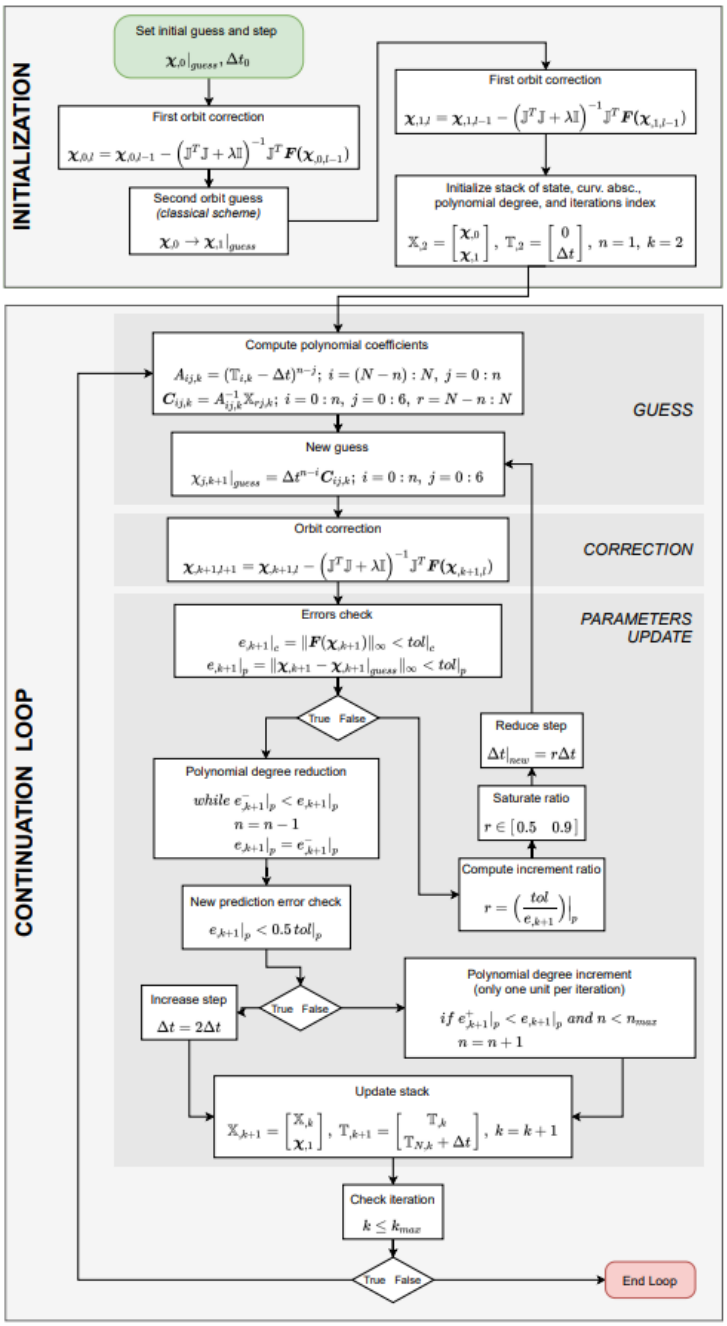

Figure A.1: QPOFs Continuation algorithm

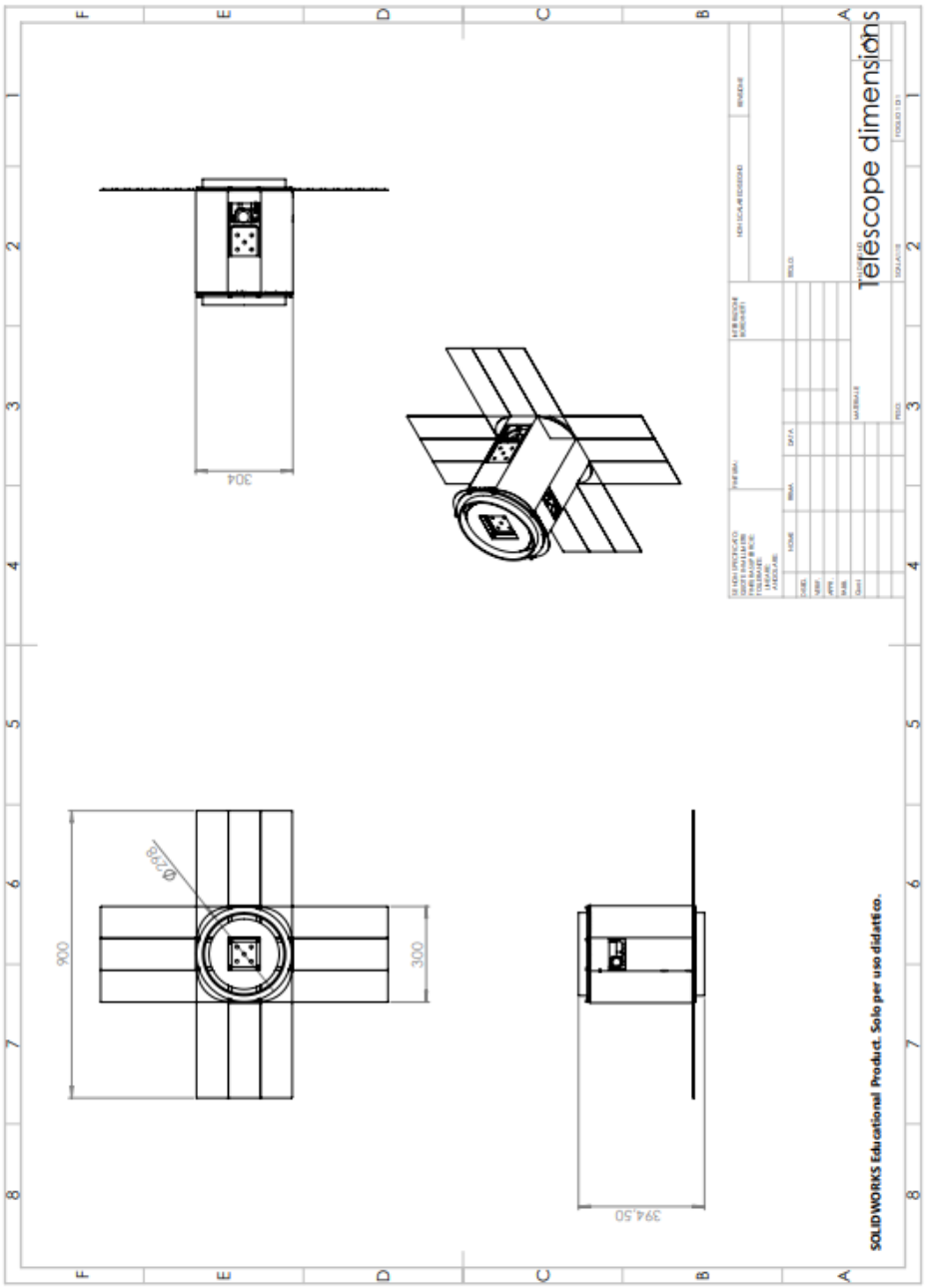

Figure A.2: ECLIPSIS Telescope dimensions

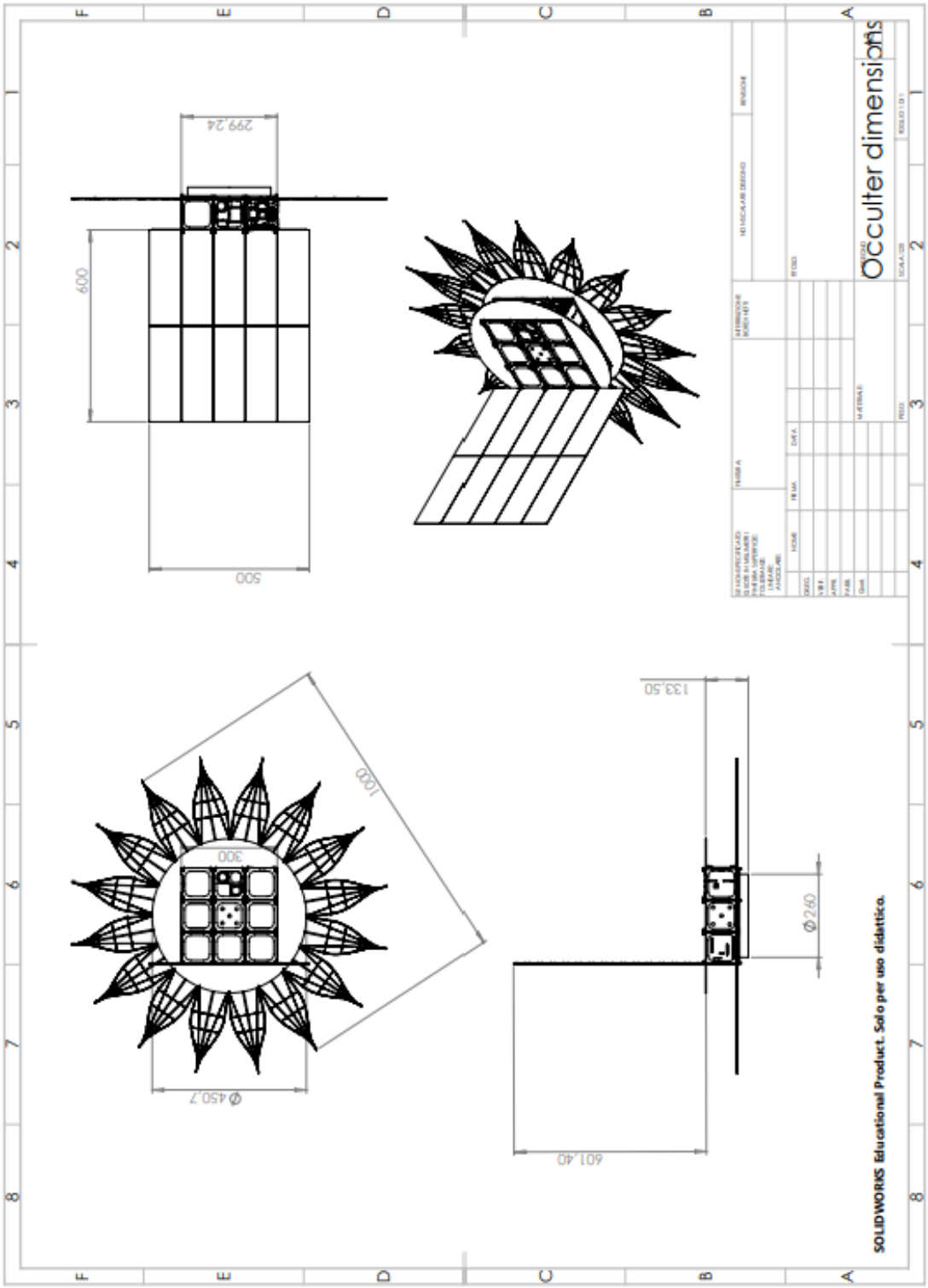

Figure A.3: ECLIPSIS Occulter dimensions